Complex electron and positron phases at the Φ-Factory DAΦNE

Gianluigi Zangari del Balzo (gianluigi.zangaridelbalzo@gmail.com)
Sapienza University of Rome

Research Article

Keywords: synchrotron radiation, category calculus, complex systems

Posted Date: May 27th, 2020

DOI: https://doi.org/10.21203/rs.3.rs-31213/v1

Complex electron and positron phases at the Φ-Factory DAΦNE.

Gianluigi Zangari del Balzo*
Sapienza University of Rome

Particle accelerators play a fundamental role in many technological and scientific fields, both for fundamental research, as in the case of high-energy physics, and for interdisciplinary applications, such as in the case of synchrotron radiation sources or proton accelerators in medical field.

Most accelerators have a critical frequency in the X-ray region: for example, in the case of the Φ-Factory DAΦNE at Frascati National Laboratories, λ_c falls into soft X-rays, for a wavelength of about 6 nm. This feature is important for diagnostic applications that generally employ frequencies in the visible region, where it is easier to design focusing optics.

This work concerns the discovery of a time-domain "anomaly" in the Infra-Red synchrotron radiation emitted by electrons and positrons from both the DAΦNE Φ-Factory (Frascati National Laboratories, Italy) and HFL (Hefei Light Source at NSRL(National Synchrotron Radiation Laboratory, People's Republic of China).

The study was conducted with an unconventional statistical category calculus system, developed and patented by the present author for the analysis of complex systems.

The "anomaly" has been resolved in the IR synchrotron radiation emission profile of each single bunch of electrons and positrons, in two distinct waveforms, one of which is "delayed" by a few hundred of ps with respect to the other.

A detailed and in-depth analysis excludes that the anomaly is the result of systematic errors

The measured time differences between the two signals leads to an apparent discrepancy in the value of the speed of light in vacuum.

A study of the anomaly with time series, based on considerations about the coherent emission of synchrotron radiation (CSR), allows us to exclude the validity of the "rigid bunch" model (J. Schwinger 1945)

We therefore propose a model called "CFNM" (Coherent Fractal Nematic Mesophase), based on considerations of statistical mechanics of complex systems, exploiting the (strong) analogies with the nematic mesophase of liquid crystals.

This model could have significant consequences in the study, modeling and measurement of the operating parameters of future machines and collectors of accelerators, in particular with regard to emission and brightness.

I. FOREWORD

When I started working as an associate researcher (theoretical physicist) at the Research Division at Frascati National Laboratories (LNF), I was asked to analyze the data of an experiment set up by the fifth scientific commission of the National Institute of Nuclear Physics (INFN), called "3+ L". This experiment was aimed at carrying out a real-time beam diagnostics for the Φ-Factory DAΦNE, but had been abandoned and closed by the Accelerators Division of the Frascati Laboratories because conventional data analysis had led to nothing. It was therefore entrusted to me because I had developed an unconventional statistical calculus system based on categories, a sort of "extension" of Set Theory. The work has continued to this day, revealing unexpected and interesting aspects.

II. INTRODUCTION

Particle accelerators play a fundamental role in many technological and scientific fields, both for fundamental research, as in the case of high-energy physics, and for interdisciplinary applications.

One of the crucial fields concerning the activity, performance and safety of accelerator machines is the diagnostics of particle beams, both for large circular colliders designed for high energy physics such as LHC, and for the accelerators dedicated to the production of synchrotron radiation.

Beam diagnostics is a "tool", or rather, a complex of methods and technologies for the operation of these important and expensive machines, since it allows us to monitor the properties of the particle beams in order to improve their performances.

Among the various processes concerning accelerator physics and, in particular, those dedicated to the monitoring and study of particle beams, one of the most important topics concerns the analysis of the emission of the radiation field generated by accelerated charged particles.

Synchrotron radiation is typically extracted from a bending magnet through a special optical window and then transmitted, along a dedicated beamline, to a complex of detectors that measure specific and observable characteristics of the source itself. The advantages of a direct use of synchrotron radiation in diagnostics lie in the following specific features:

* gianluigi.zangaridelbalzo@gmail.com

1) it is a very reproducible and characterizable (with high precision) source;
2) it is a not invasive and / or destructive source for the particle beam, therefore it is ideal for diagnostics;
3) it is a source distributed over a wide spectrum of radiation (from far IR to X-rays). Consequently, the photon energy can be chosen based on the type of diagnostics and the characteristics of the detectors;
4) it is a highly collimated source with a well-defined angular divergence;
5) it is a very bright source;
6) it is a source that has a well-defined temporal structure, which depends directly on the longitudinal dimensions of the beam.

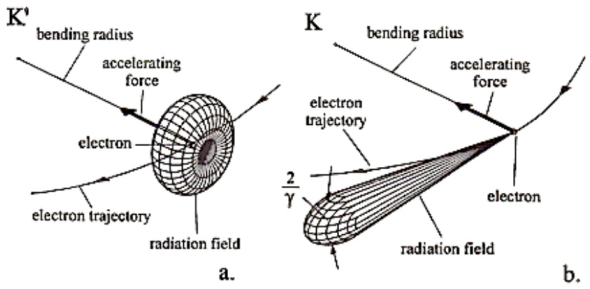

FIG. 1. Distribution of the synchrotron radiation field in the center of mass system (a) and in the laboratory system (b). Note the very directional distribution, extended in a cone with an amplitude approximately equal to 1 /γ (b). Courtesy of K. Wille [1]

One of the most important characteristics of synchrotron radiation, hereinafter abbreviated as "SR", lies in the peculiarities of the emission spectrum. In the case of particles accelerated by a bending magnet with radius ρ, SR is characterized by a critical wavelength λ_c which divides the integral of the power radiation into two equal parts. For the frequencies $\lambda << \lambda_c$ the power spectrum of the radiation tends rapidly to zero while for $\lambda >> \lambda_c$ the power spectrum is almost constant and, therefore, approximately independent of the energy of the particles.

Most accelerators have a critical frequency in the X-ray region: for example, in the case of DAΦNE, λ_c it falls into soft X-rays, with a wavelength of about 6 nm. This feature is important for diagnostic applications that generally employ frequencies in the visible region, where it is easier to design a focusing optics.

SR is used both to carry out longitudinal diagnostic measurements of the beam, and to obtain information on its transverse size.
In a circular accelerator the particles are distributed in "packets" ("bunches") with a well-defined time structure. The longitudinal distribution of the particles can be detected by the temporal structure of the radiation emitted by single bunches. In this case, important information on the longitudinal dynamics of the beam can be obtained, as well as on the profile and length of the single bunches. It is also possible to measure important parameters (i.e. the impedance of the machine) and study the longitudinal instabilities of the beam. However, this type of diagnostics requires the use of fast detectors. For example, to resolve an electron bunch with a size of the order of 1 mm, the detectors must exhibit temporal responses in the order of the ps.

The spectral distribution of SR does not depend on the energy of the machine, but only on the radius of curvature of the bending magnet and on the current injected into the accelerator. The power extracted by a bending magnet at certain wavelengths is therefore comparable in almost all accelerators, allowing, in principle, the use of a certain diagnostic in all machines.

One of the limitations of the current transverse diagnostics with SR sources, lies in the time resolution for the acquisition of images, limited to the order of 30 ms for standard video cameras. This limit prevents turn-by-turn diagnostics, since the time of a revolution for almost all colliders is of the order of μs (for example the revolution time in DAΦNE is about 32 μs). Furthermore, to monitor the transverse size bunch-by-bunch, the time response of a detector should be less than ns (for DAΦNE the distance between two consecutive bunches is about 2.7 ns). Some bi-dimensional sensors have characteristic acquisition times of 104 - 105 frames/s: a turn-by-turn diagnostics is thus able to achieve only a limited number of pixels of the matrix, for example 64 x 24 pixels at 105 frames / sec for a typical LHC beam monitor device at CERN [2] . However, these (VIS) sensors do not allow to solve bunch-by-bunch emission because they are limited both in exposure times and in sensitivity.

Bunch-by-bunch and turn-by-turn beam diagnostics are fundamental for studying beam instability phenomena. In recent years, the diagnostic systems installed at SLAC (Stanford) [3] or at the Japanese KEK [4] , used assembled devices made by a MCP ("Microchannel Plate Detector"), a fluorescent screen and a CCD ("Charge-Coupled- Device"). These systems helped to study and identify beam instabilities due to "electron clouds", therefore characterizing the transverse dimension of the beam bunch-by-bunch. However, they did not allow to obtain a synchronous image of all the bunches in the beam because they were limited by the frame rate of the CCDs used.

In our case, the above problems were addressed by using ultrafast uncooled photodetectors based on HgCdTe (MCT) hetero-structures. MCT detectors represent valid and competitive elements, capable of replacing - or in any case supporting - the "old" streak cameras, certainly more expensive, complex and delicate.
MCT detectors were used to monitor DAΦNE electron / positron beams in order to obtain a "real-time" diagnostics, because they can provide an analysis turn-by-turn and "bunch-by-bunch".

MCT detectors can follow the longitudinal dynamics, as well as they can identify, monitor and characterize the instabilities of the beam and the individual packets, improving the accelerator performance (i.e. maximum cur-

rent and brightness). We will return later with a paragraph dedicated specifically to these detectors.

The tests were conducted on both DAΦNE and HFL (Hefei Light Source) of the National Synchrotron Radiation Laboratory (NSRL) of the People's Republic of China.

Finally, the response of the MCT photo-detectors used was analyzed with the unconventional statistical category calculus system, developed and patented by the present author in 1997-99, which we will discuss below.

III. THE Φ-FACTORY DAΦNE AT FRASCATI NATIONAL LABORATORIES

DAΦNE is a double collision ring for electrons and positrons of 0.51 GeV per beam. The total energy, equal to 1.02 GeV, corresponds to the mass of the particle ϕ. To decrease the interactions between the beams, the electrons and the positrons circulate in opposite directions in two distinct rings that cross at two interaction zones (KLOE and FI.NU.DA). To avoid the collisions of the beams with the residual gases, a particularly high vacuum is maintained in the rings (less than a thousandth of a billionth of atmospheres). In the DAΦNE rings, about 100 m long, circulate more than 100 bunches consisting of more than 100 billion particles that perform more than 3 million revolutions in a second and whose collisions produce about 2000 ϕ particles per second.
The dimensions of each bunch at the interaction point are 1mm x 10μm x 2cm.

As shown in figure 2 above, the DAΦNE injection system consists of a linear accelerator (LINAC) of about 60 m, an almost octagonal intermediate storage ring with a total length of about 32.5 m and about 180 meters of transfer lines from LINAC to the accumulator and from these to the two main rings (see figure 3 below), terminated in the two interaction zones (KLOE and FI.NU.DA).

The Luminosity is given by

$L = \frac{N^{e^+} N^{e^-}}{4\pi\sigma_x\sigma_y} f = 10^{32} cm^{-2} s^{-1}$

where for DAΦNE we have:

$N^{e^+} \approx 2 \cdot 10^{10} positrons/bunch$

$N^{e^-} \approx 2 \cdot 10^{10} electrons/bunch$

$\sigma_x \approx 1mm$ average quadratic horizontal dimensions in the IP (Interaction Point)

$\sigma_y \approx 10\mu m$ average quadratic vertical dimensions in the IP

$f = 3 \cdot 10^8 s^{-1}$ collision frequency

IV. THE EXPERIMENT "3+L" AT FRASCATI.

The experiment called "3 + L" (Time Resolved Positron Light Emission) had unique characteristics among the DAΦNE beam diagnostics techniques, because it wanted to carry out, for the first time, real-time

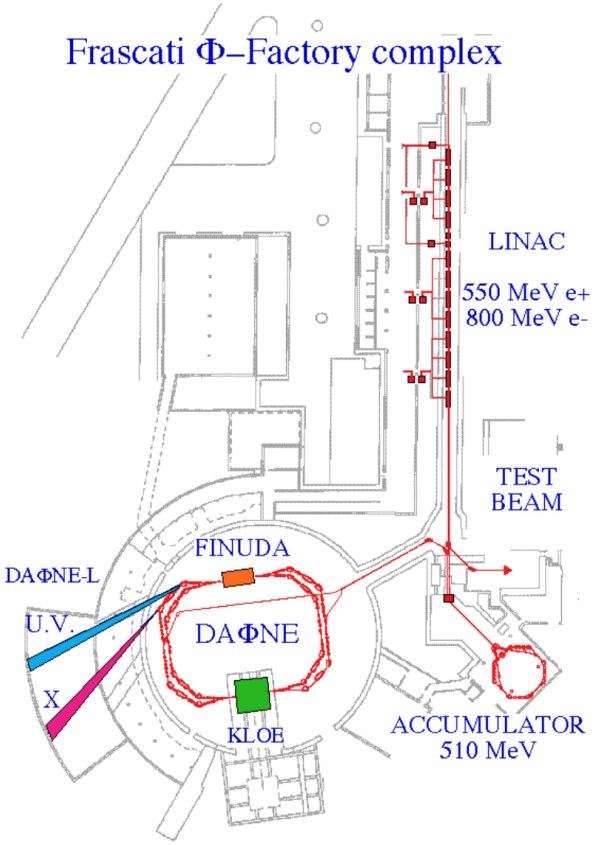

FIG. 2. Schematic of DAΦNE injection system (courtesy of Frascati National Laboratories).

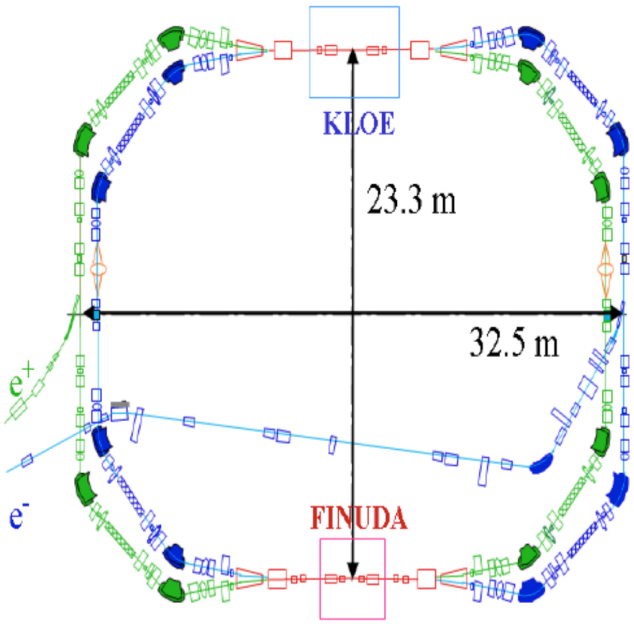

FIG. 3. Schematic of the two main rings of DAΦNE (courtesy of Frascati National Laboratories)

beam diagnostics, capable of characterize each bunch of particles ("bunch-by-bunch") with a compact and contained tool, both in size and in production costs. The experiment used ultra-fast MCT detectors at room temperature.

In the figures 4-5 is represented the arrangement of the experiment "3 + L" [5, 6] . MCT detectors used by the experiment had been tested on DAΦNE's dedicated SINBAD (Synchrotron Infrared Beamline at DAΦNE) infrared beamline, and on the dedicated HLS (Hefei Light Source) IR beamline at the NSRL (National Synchrotron Radiation Laboratory) facility (Hefei, People's Republic of China).

V. ULTRA-FAST MCT PHOTO-DETECTORS.

The ultra-fast photo-detectors used both at Frascati and Hefei are made by HgCdTe (MCT) hetero-structures by the Polish company VIGO System SA [7, 8]. MCT detectors operated at room temperature with a rapid response in an interval of the order of hundreds of ps. The compounds of HgCdTe, cadmium telluride and mercury (or cadmium telluride, mercury, MCT or CMT) are CdTe and HgTe alloys which represent the third semiconductor for technological importance after silicon and gallium arsenide. The quantity of cadmium (Cd) in the alloy can be chosen in order to optimize the optical absorption of the material at infrared (IR) wavelengths. CdTe is a semiconductor with a prohibited band of about 1.5 eV at room temperature while HgTe is a semi-metal with zero band gap energy. The mixture of these two compounds allows, in principle, to obtain a compound with a variable gap between 0 and 1.5 eV. MCT compounds are among the few materials capable of detecting infrared radiation in both accessible atmospheric windows, i.e. between 3-5 μm (MWIR) and 10-12 μm (LWIR).

The detection in the MWIR and LWIR windows is generally obtained by using the compounds [($Hg_{0.7}Cd_{0.3}$) Te] and [($Hg_{0.8}Cd_{0.2}$) Te] respectively. A MCT detector is also capable of detecting radiation through atmospheric windows of 2.2-2.4 μm and 1.5-1.8 μm (SWIR). Due to their extraordinary operational peculiarities, MCT detectors have been largely used in military applications for night vision, aeronautical use, satellite observation and missile guidance, in particular for the so-called "smart bombs". Large varieties of heat-seeking missiles are still equipped with MCT detectors. Today these detectors are widespread used in almost all fields of research. Many detectors even take their name from astronomical observatories (i.e., Hawaii) or from the instruments for which they were originally developed.

In this case, the MCT detectors made by VIGO System SA represent the current state of the art of MCT technology by virtue of the operation at room temperature, the rapid response and contained costs. The MCT detectors of the "3 + L" experiment were used both as single elements and in a compact two-dimensional matrix consisting of two arrays of 32 elements with a response of the order of ns. (See next figures 6-7).

The realization of these photo-detectors was carried out using 3-phase Photo Voltaic Multiple Junction (PVMJ) technology which employed straight MCT (HgCdTe) structures grown with MOCVD (Metal-Organic Chemical Vapor Deposition) technology on direction-oriented GaAs substrates (211) and (111) [7, 8] . The detectors are optimized to work in the MIR (middle IR $\simeq$10.6 μm). Their typical response time did not exceed 100 ps during tests carried out under cooling at 205 K with a three-stage Peltier cell [7, 8] . The detectors were inversely polarized and each coupled to a broadband preamplifier in order to optimize its performance and improve its S/N ratio. To this end, an amplifier characterized by a gain of 46 dB and a bandwidth between 0.1-2.500 MHz was used [7, 8] . Given the high sensitivity of the devices, to shield the RF signal of the DAΦNE klystron, both the arrays (See fig. 7) of the photo-detectors and the amplifier were isolated inside a metal box [5–8] .

These peculiarities make the MCT detectors ideal for analyzing the synchrotron radiation of high current accumulation rings (about 2A) - typical of DAΦNE operating regime - and are therefore suitable for performing effective beam diagnostics. In the experimental arrangement at room temperature, the rapidity of the response time allowed to obtain an excellent temporal resolution of the synchrotron emission signal of each bunch of electrons and positrons for each complete injection cycle.

The first tests of the photo-detectors were carried out in the IR line SINBAD (Synchrotron Infrared Beamline at DAΦNE) by initially studying the response of an individual detector and then of single elements ("single channel") of an array and, subsequently, a set of elements (4) activated on the matrix 32x2 of MCT photodetectors, indicated in red in the figure 6 above [5, 6] .

In the following of this work, the four elements activated on the 32x2 matrix will be indicated as "pixel", hence "pixel1", "pixel2", "pixel3" and "pixel4" (See figure 6).

VI. DATA ANALYSIS.

Data analysis was performed by the SHT category calculus system, developed in the context of Category Theory in 1997 and patented since 1999 by the present author for the study of complex systems.

Initially, my goal was to "categorize" data analysis processes as an algorithm and thus achieve complete automation. In the following years, the progress of age (and experience) convinced me that total automation is dangerous because it can cause and introduce serious systematic errors, especially in the study of complex systems or far from thermodynamic equilibrium. So I resumed the habit of manually rechecking the results of the various levels of analysis. Even in the case of powerful computers

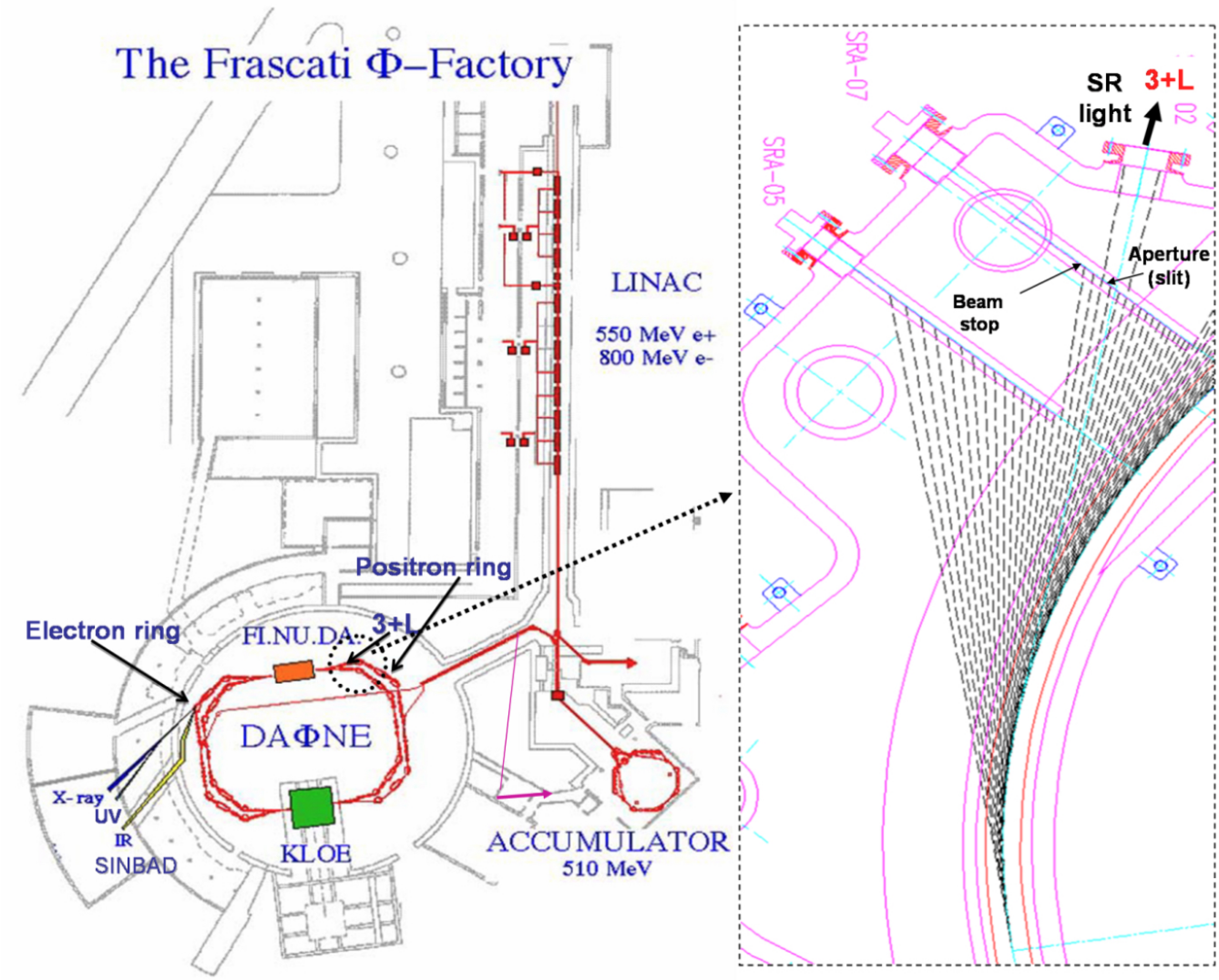

FIG. 4. Layout and arrangement of experiment 3 + L at DAΦNE (courtesy of Frascati National Laboratories)

and large data sets (such as in Frascati or CERN) and for processes based on artificial intelligence or machine learning algorithms. In all these cases, paradoxically, I noticed that human intervention is fundamental because errors are always there and tend to spread diabolically. From which I am convinced of the irresponsibility and the danger of letting a machine, however sophisticated, have full control of a process. This should be considered not only in research, but also in civil automation (airplanes, automobiles, surgical robots, etc.). The ghost of Hal9000 is unfortunately always around the corner!

For this reason, I gave way to the control of a human operator during the phases and levels of the analysis, however trying to avoid that the human operator could violate the Method's conditions of reproducibility and inter-subjectivity. For example, in the present case, there are no tunable parametric models, such as the Hodgkin-Huxley models for the generation of nerve impulses [9] . The operator can follow the development of the various levels and verify that the results adhere point-by-point to reality. If the result of the process differs significantly from the experimental data, the system will stop and catalog it as a "scenario", assigning it a probability. In this case, the system will search for the most likely scenario. To be honest, in SHT analysis there is a very strong integration between man and machine, a sort of true symbiosis, in the sense that the operator's human brain is an "integral part" of the machine's mathematical algorithms. It is a bi-univocal process, because mathematical algorithms exploit the capabilities of the human brain, while the human brain takes on the Method's rules of reproducibility and inter-subjectivity as if it were a machine! I understand that it is not easy to explain in a few lines, but the example covered in this work should clarify my thinking. For any further clarification, See [10]

From the practical point of view, SHT analysis did not

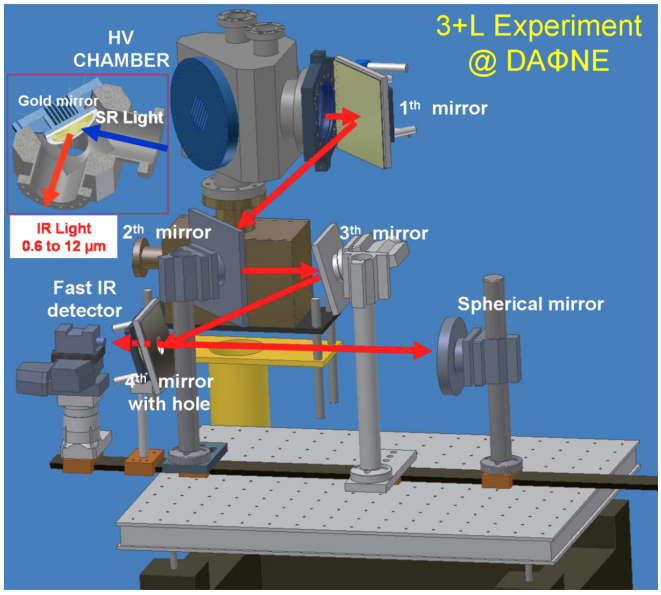

FIG. 5. Optical layout of the experiment 3 + L with the "front end" structure, the optical table, the mirrors and the IR detector. The ideal path of IR radiation, from input to focusing optics is shown in red (courtesy of Frascati National Laboratories).

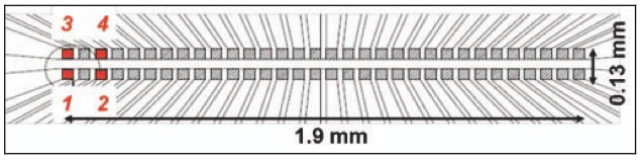

FIG. 6. Matrix structure of MCT detectors with 4 activated channels (in red) (courtesy of Frascati National Laboratories and VIGO System SA [7])

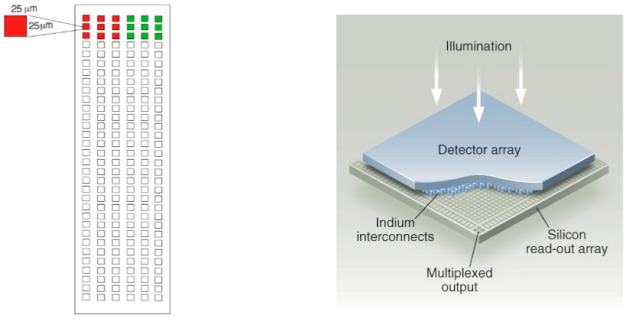

FIG. 7. (Left) Optimized topology for a MCT detector matrix. (Right) Detector "anatomy" (courtesy of Frascati National Laboratories and VIGO system SA [7])

FIG. 8. SHT category calculus logo

take place either with changes to the sample, or with reductions or subtractions of any kind: the SHT algorithms analyzed the system *sic rebus stantibus*, also considering the "junk". I think it was almost certainly for this reason that I was entrusted with this job, because the "3 + L" data had previously been identified as junk and archived, if not to say, trashed!

SHT looks for, if it exists, a partition of each data ensemble, considered as a sort of "dynamic system". In the affirmative case, the dynamic evolution of the data around the attractors is studied. In this way, it is also easier to identify any systematic errors!

If SHT manages to identify an attractor, it will become a "category" of the experiment in question. But only of that particular experiment. Once the possible categories have been identified, SHT looks for, if it exists, a subset of "morphisms" that possess the qualities of probability functions. In this case, SHT defines these morphisms as "maximum congruence profiles".

From an implementation point of view, SHT analysis was performed through algorithms designed and adapted *ad hoc* in the mainframe data center machine codes (in this case, the main routines were installed as "open source" in the Frascati data center) and, from time to time, they are translated into programming and compilation through human interfaces of commercial software such as "Matlab", "Origin", "Mathematica", "Kaleidagraph", etc.

The analysis is conducted on nine levels. Levels 1, 5 and 9 are the most important. Level 1 restore, rebuilds and catalogs the data, trying to bring order to the initial chaos. Levels 5-6 sorts the data in time series, level 9 processes the maximum congruence regressions. The intermediate levels are dedicated to the declaration of variables, labeling ("tagging"), to the reconstruction of time intervals and delays ("lagging"), calibration in time (or "bunch number") and so on.

In the following sections I will give a practical example,

trying to summarize the main levels and their results with diagrams.

VII. FIRST LEVEL SHT ANALYSIS: MATCHING.

The optimization procedures of the first level of analysis made it possible to collect and generate groups of experimental data by selecting the relative configurations of the databases found and restored. This made it possible to cope with the total lack of references and information. The declarations and labels of the variables ("taggings") were in fact devoid of references to measuring devices, zeros and gauges. The analysis was therefore performed by arranging the data in a sort of rugged funnel by Hans Frauenfelder [11, 12] , called "Data-Funnel" (configuration entropies vs signal/noise ratio, See the following figures). This procedure thus avoided the subjective introduction of selection criteria. The ultimate goal of the SHT first level processes was to create a "cladistics" of experimental data. The following figures 9-12 show some pairs of selection examples with data-funnels for electron emissions (9-10) and positron emissions (11-12).

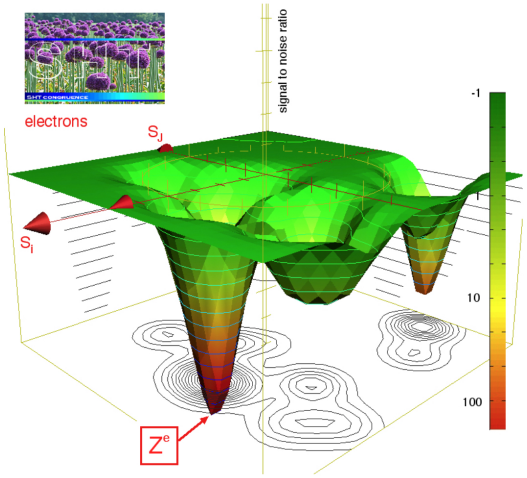

FIG. 9. Level 1 - Data-Funnel of an ensemble of matrices relating to DAΦNE electron synhcrotron radiation emission data. The absolute minimum Z^e identifies the best values of the ensemble.

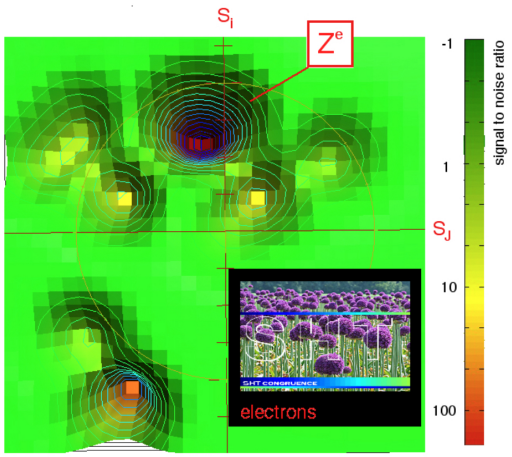

FIG. 10. Level 1 - Data-Funnel section of the same ensemble of matrices (see fig. 9) relating to DAΦNE electron synhcrotron radiation emission data. The absolute minimum Z^e identifies the best values of the ensemble.

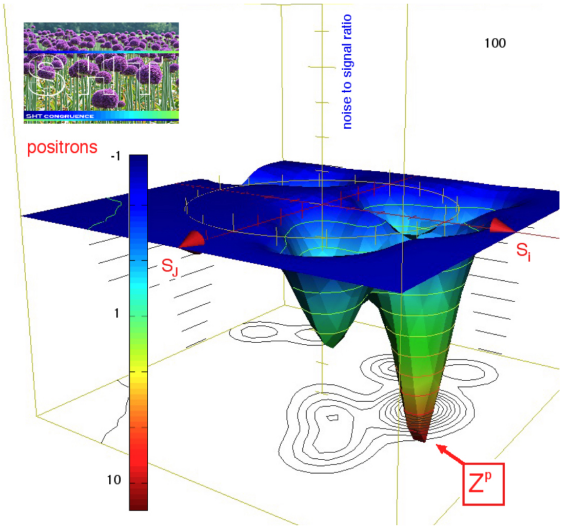

FIG. 11. Level 1 - Data-Funnel of an ensemble of matrices relating to DAΦNE positron synhcrotron radiation emission data. The absolute minimum Z^p identifies the best values of the ensemble.

VIII. LEVELS 2-4 SHT ANALYSIS: VARIABLE TAGGING, TIME LAGGING AND MCT TIME CALIBRATION.

For the calibration in time (ns) of the response of each photo-detector, I started from the constructive and operational parameters of DAΦNE

I considered the period of a complete cycle of filling 100 bunches of particles in DAΦNE, equal to

TABLE I. DAΦNE constructive and operational parameters (courtesy of Frascati National Laboratories)

DAΦNE constructive and operational parameters	
Diameter (m)	97.588664
RF (MHz)	368.664
Harmonic Number	120

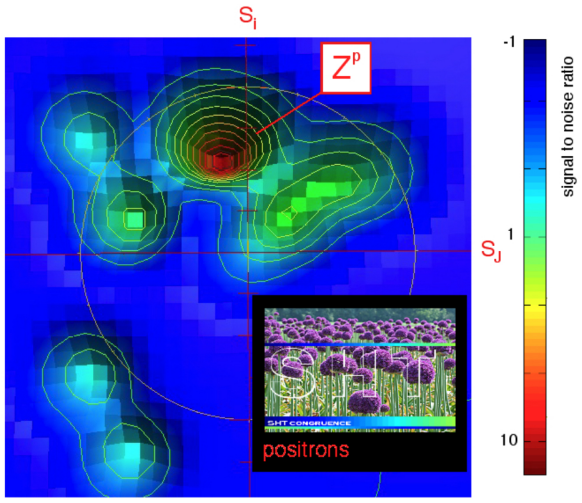

FIG. 12. Level 1 -Data-Funnel section of the same ensemble of matrices (see fig. 11) relating to DAΦNE positron synhcrotron radiation emission data. The absolute minimum Z^p identifies the best values of the ensemble.

$T = \frac{1}{RF} \cdot 120 \simeq 325.499642\ ns$

corresponding to a bunch separation of about 2.7 ns.

The first thing that catches the eye of the above diagrams is the anomalous (See also A. Hofman [13]) complex profile of the synchrotron radiation signal of each bunch, both for the emission of electrons and for that of positrons, which seems to be the result of the convolution of a "fast" term, which we will call "main", with a "delayed" term.

Of course, I immediately thought that this "anomaly" was a systematic error of the measuring apparatus. Checks on the data and on the measuring device excluded this possibility. The measurement was in fact repeated with various modifications of the apparatus and conditions, also changing the MCT detectors. Furthermore, it was also performed on the Chinese Hefei synchrotron. In all cases, the anomaly remained, changing only in intensity, width and center. We will come back to this later.

Let's go to the end, moving immediately to the regression of the two terms, "main" and "delayed", then we'll go back to the analysis of the time series.

IX. LEVEL 9 SHT ANALYSIS.

The intensity measurements of each emission peak were carried out by SHT level 9 regressions on the IR-SR (infrared synchrotron radiation) emission profile of each bunch, distinguishing, from time to time, the contributions of the two terms, respectively "main" and "delayed". In this way, I have avoided a serious systematic error of most spectral analysis software (eg "peakfinder", "peaks" and so on), which is blind to the (hidden) components in the convolution (see figure 15). Similarly, the separation of the analysis into two components, which I call "dichotomous analysis", allows me to avoid that the study of the "main" profile is influenced by the "delayed" component. It is an important step to underline and remember in case the delayed component is caused by a systematic error of the apparatus (which is not).

The measurement of the time intervals (and the relative delays) must also be correct. We will need it in the time series (See next fig. 16 and the next section about "time series").

The following figures show some level 9 Gaussian regressions of the double profiles ("main" and "delayed") for DAΦNE electrons and positrons.

Figures 17 to 20 show 4 double regressions typical of the synchrotron radiation emitted by a single bunch of DAΦNE electrons, acquired by 4 photo-detectors (called "pixels") activated on the matrix (see figure 6), while figure 21 represents a double regression of the synchrotron radiation emitted by a single bunch of DAΦNE positrons acquired by a single photodetector.

X. LEVEL 5-6 SHT ANALYSIS: TIME SERIES.

My decision to use time series analysis in accelerator and particle physics was perhaps a bit extravagant but, in a certain sense, it was forced precisely by virtue of the peculiarity of the time response of MCT detectors, capable of analyzing IR emission of synchrotron radiation by discriminating each bunch of particles (also thanks to the statistical analysis SHT used).

The objective of our analysis concerns the time evolution of electron and positron bunches through the study of the synchrotron radiation emitted. This is our phenomenon Z (t). I have thus an ordered collection of a sequence, not necessarily regular, of x_t observations

$Z_t = \{x_t;\ t = 1, ..., N\}$

Therefore, I am interested in defining a historical series Z_t as the linear composition of a non-stationary deterministic process Y_t - possibly attributable to a *trend* component - with a purely random erratic process or "white noise" [14–18] , such that

$E\left(Y_t u_t\right) = 0$

With reference to figure 16 above, consider the ensemble averages on the synchrotron radiation emission intervals of each bunch for each configuration (d,j), where d,j = 1,....,p with p∈ℕ the total number of the configurations

$\triangle t = \left\langle \triangle t_j^d \right\rangle_{dj} = (2.7 \pm 0.4)\ ns\ ;\ d, j \in \mathbb{N}$

which overlaps with the expected value of the separation ("bunch separation"), calculated from the operational and construction values of DAΦNE. The error is the result of the averages of ensemble from level 9 regressions[19] .

Then, we define an index variable t∈ℕ called "bunch-number", as follows:

$\triangle t\,(ns) \in \mathbb{R} \rightarrow t\ \ (bunchnumber) \in \mathbb{N}$ where t = 1,....., T (bunch-number). Then, the correlogram of the Z_t series, generated from the correlations between the same and each delayed series of k periods, represents

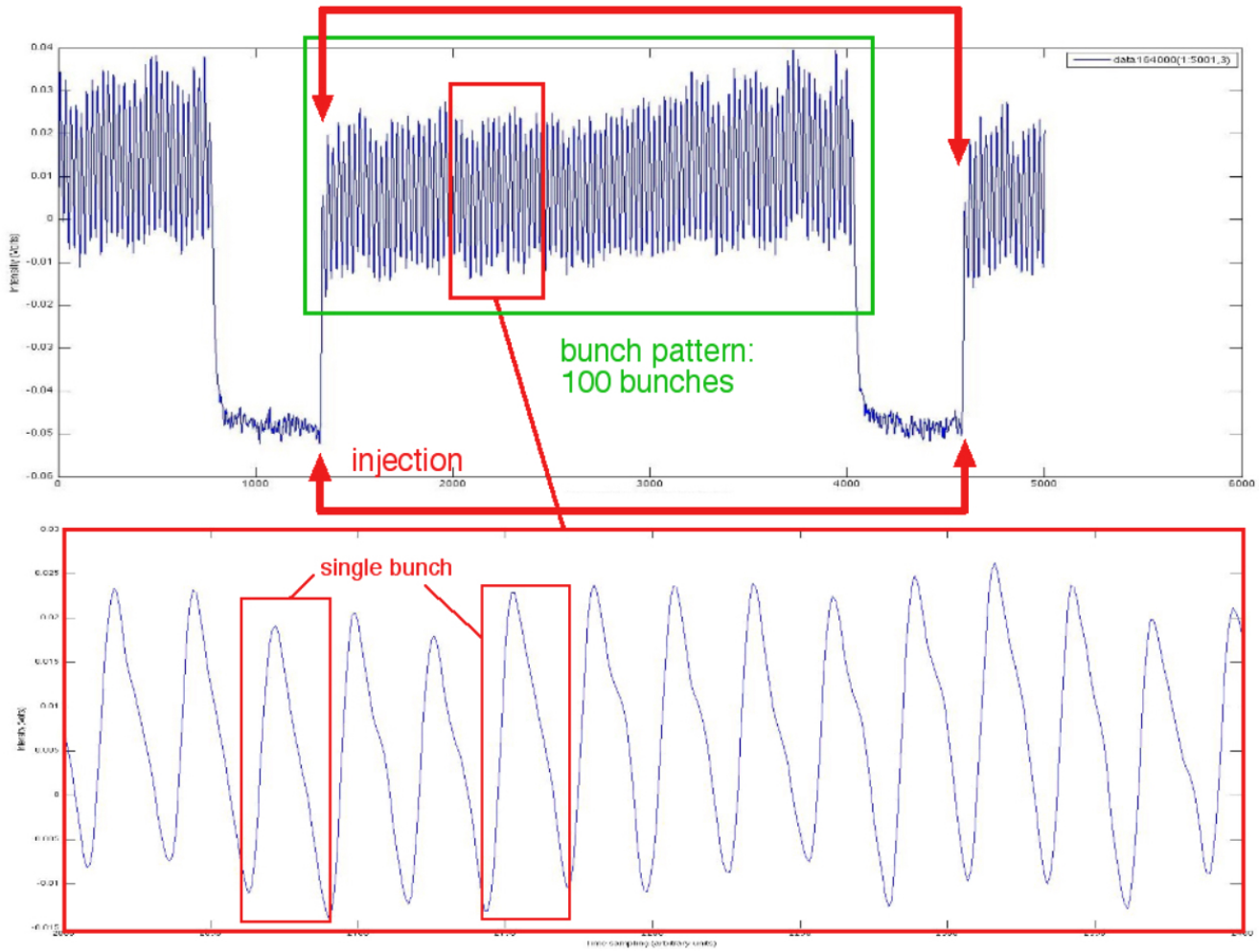

FIG. 13. Typical signal of the IR synchrotron radiation emission photo-detector response, corresponding to a complete filling of 100 bunches of DAΦNE electrons (highlighted by red arrows).

the variation of the self-correlation ρ (k), taken from the following relationship

$$\rho(k) = \frac{cov(Z_t, Z_{t-k})}{\sigma_t \sigma_{t-k}} = \frac{\sum_{t=K+1}^{T} (Z_t - \overline{Z}) \cdot (Z_{t-k} - \overline{Z})}{\sum_{t=K+1}^{T} (Z_t - \overline{Z})^2}$$

where in the present case the comparison was made between series of equal length, i.e. for T = 100 and K = 99.

The following figure 22 shows the result of the calculation for the best ensembles of the "main peaks" acquired by each of the 4 (pixels) (DAΦNE electrons).

From a quick look at figure 22, a pair by two between the response of the photo-detectors, 1-2 (green-violet) and 3-4 (orange-blue) respectively, is evident. This is valuable information linking the topology and alignment of the detector to the emission profile of synchrotron radiation (intensity). It will be very useful for future detector matrix design (see Figure 6 above) in order to perform synchrotron light imaging (this is a very interesting application, which I developed separately).

Now we can proceed with the representations of the results.[20]

The correlation analysis of the time series Z_t is a necessary condition to the decomposition operations and, therefore, to the estimation of the trend model, as well as useful to reveal the possible emergence of other factors (for example the "seasonality") eventually superimposed on the dominant component.
The first significant "marker" of the correlogram (highlighted in green in the following figure 24) was chosen to represent the autocorrelation in correspondence of the delay at T/4 ("boundary lag"), ie for k = 25.
Therefore, I decided to extend the calculation of the ζ-th quantile of the normal standard to 1.96 ($\zeta = 0.975$) over the entire range of variation of the series, taken from

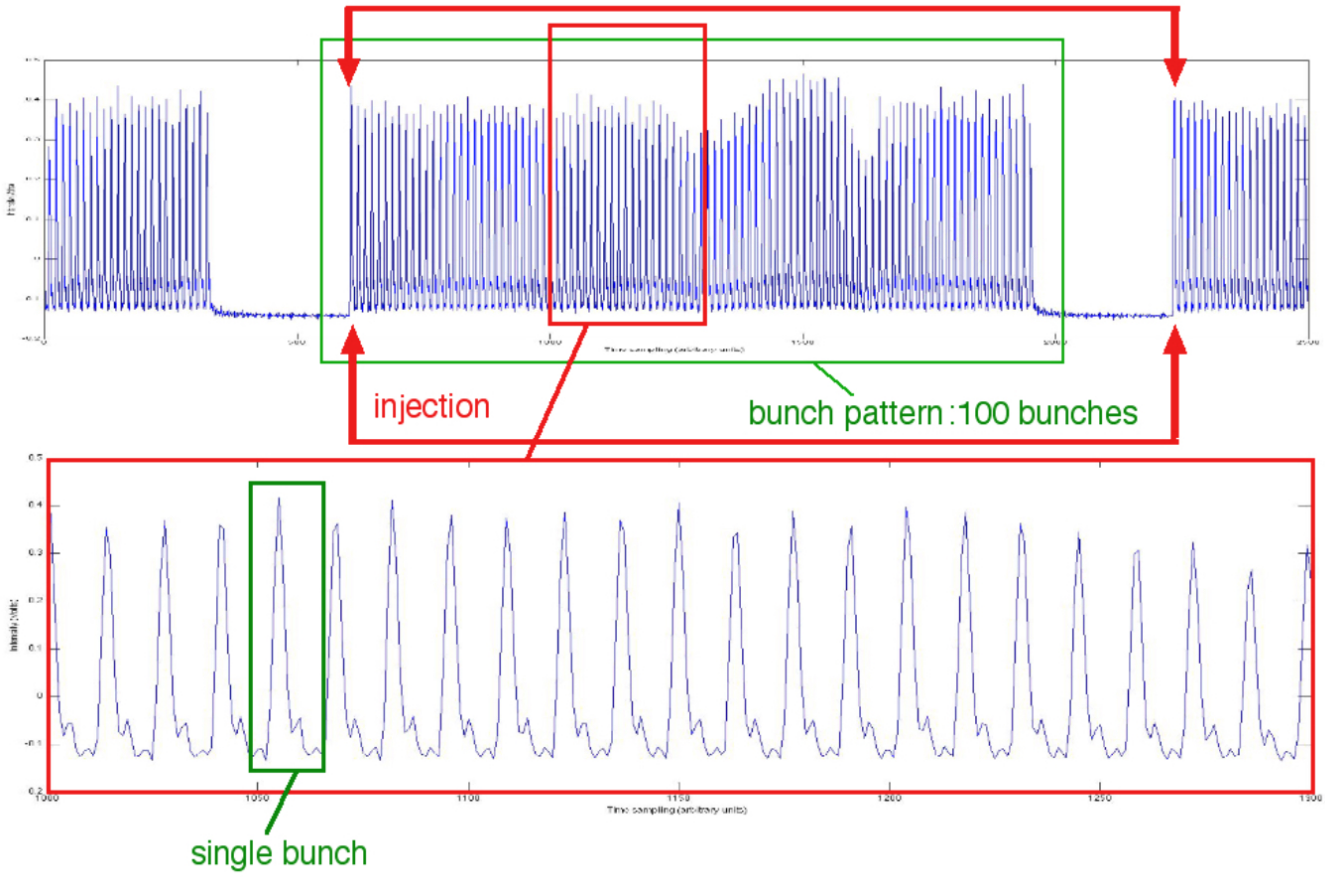

FIG. 14. Typical signal of the IR synchrotron radiation emission photo-detector response, corresponding to a complete filling of 100 bunches of DAΦNE positrons (highlighted by red arrows).

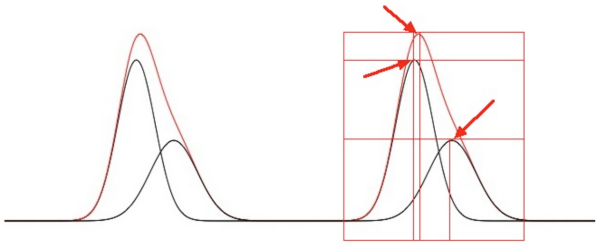

FIG. 15. Typical systematic error of the automatic tool "peak-finder", offered by commercial spectral analysis software. The software is blind to the components (hidden) in the convolution (black), so it overestimates the intensity and misses the width and the center.

the period of a complete filling of electron bunches in DAΦNE (T = 100) from which we have the following confidence interval

$$\left[-\frac{z\left(1-\frac{\alpha}{2}\right)}{\sqrt{N}}, \frac{z\left(1-\frac{\alpha}{2}\right)}{\sqrt{N}}\right] \cong (-0.96, 0.96)$$

where z_ζ is the quantile.

Now, consider a polinomial model $\hat{Y}_t$ and the "residuals"

$R_t^\Sigma = Z_t - \widehat{Y}_t \;\; ; \forall t$

$R_t^\Pi = \frac{Z_t}{\widehat{Y}_t} \;\; ; \; \widehat{Y}_t \neq 0 \; \forall t$

We are therefore looking for a model $\hat{Y}_t$ such that $\left\langle R_t^\Sigma \right\rangle \cong 0, \; \forall t$

So let's analyze the residual correlogram for at least four models[21] checking that the distributions are all included within the ζ-th quantile confidence bands ($\zeta = 0.975$).

As an example, in the following figure 24, I represent only the diagram for the quadratic detrend.

The following table 2 summarizes the residual statistics for four models (main component -DAΦNE electrons) .

From the previous table, I choose the quadratic model (second column)

$$Z_t \cong 0.0108 + 4.5508 \cdot 10^{-5} t \; - \; 3.4025 \cdot 10^{-9} t^2 \; + \; u_t$$

where u_t is the "erratic" component. I represent the result of the analysis in the following figure 25.

Now I repeat the same procedure for the "delayed" component. The following table 3 summarizes the residual statistics for four models ("delayed" component - DAΦNE electrons).

TABLE II. Residual statistics table for four models ("main" component -DAΦNE electrons).

Statistics	detrend poly (1)	detrend poly (2)	detrend poly (3)	detrend poly (4)
Minimum	-0.0046566	-0.004674	-0.0047491	-0.0048799
Maximum	0.0032093	0.0033188	0.0033139	0.0030894
Sum	-0.0040536	1.6101e-06	-0.0045512	-0.0039613
Points	100	100	100	100
Mean	-4.0536e-05	1.6101e-08	-4.5512e-05	-3.9613e-05
Median	0.0002379	0.00022839	0.00015566	0.00011573
RMS	0.0016476	0.0016456	0.001655	0.00011573
Std Deviation	0.0016554	0.0016539	0.0016627	0.0016358
Variance	2.7402e-06	2.7353e-06	2.7647e-06	2.676e-06
Std Error	0.00016554	0.00016539	0.00016627	0.00016358
Skewness	-0.59789	-0.60144	-0.62628	-0.55162
Kurtosis	-0.031451	-0.012196	0.10651	-0.00050476

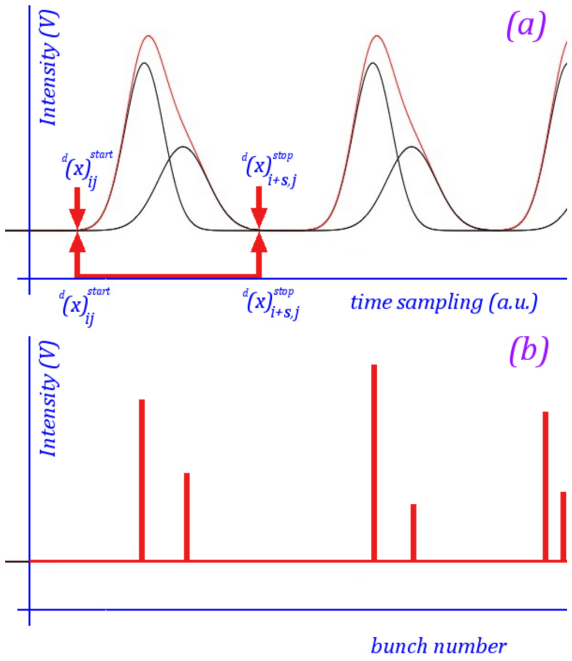

FIG. 16. Transformation of time intervals and delays. Figure (a) Sampling and definition of the time intervals between the radiation emission of each bunch (DAΦNE electrons). Figure (b) histographic sequence of intensity sampling.

As an example, in the following figure 26, I represent only the diagram for the linear detrend.

From the previous table, I choose the linear model (first column)

$Z_t \cong 0.00011 + 4.9364 \cdot 10^{-5} t \; + \; u_t$

where u_t is the "erratic" component. I represent the result of the analysis in the following figure 26.

By comparing the summary diagrams 25 and 27, I can appreciate a small variation in the trend of the delayed synchrotron emission component vs the "main" (non-linear) one.

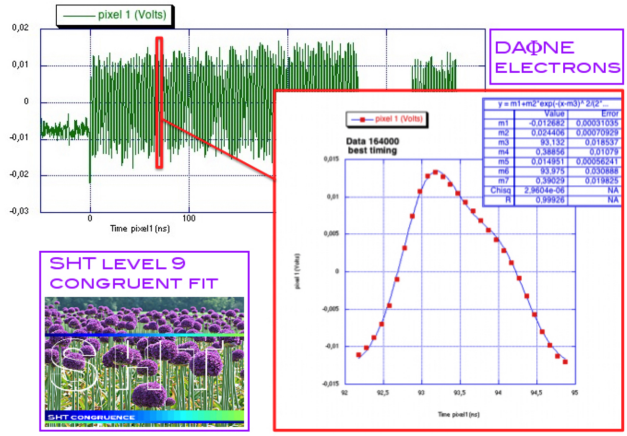

FIG. 17. SHT level 9 regression with a double Gaussian on a typical IR synchrotron radiation (pixel 1) double emission profile ("main" and "delayed") of a bunch of DAΦNE electrons.

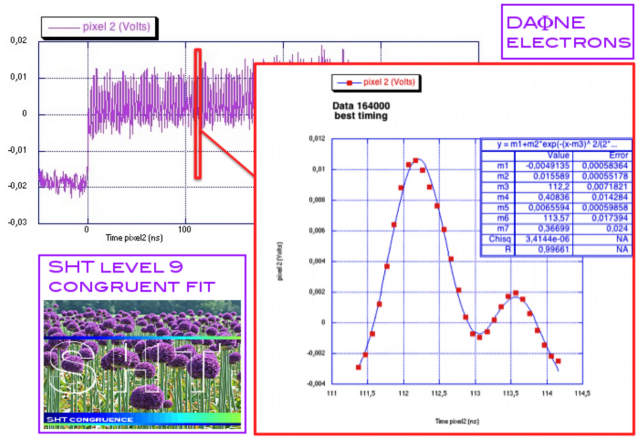

FIG. 18. SHT level 9 regression with a double Gaussian on a typical IR synchrotron radiation (pixel 2) double emission profile ("main" and "delayed") of a bunch of DAΦNE electrons.

TABLE III. Residual statistics table for four models ("delayed" component -DAΦNE electrons)

Statistics	detrend poly (1)	detrend poly (2)	detrend poly (3)	detrend poly (4)
Minimum	-0.00369556	-0.00352341	-0.00356587	-0.00386242
Maximum	0.002501826	0.002531689	0.00246456	0.002324784
Sum	-1.92376e-07	-1.55592e-06	6.90214e-06	6.082405e-05
Points	88	88	88	88
Mean	-2.1861e-09	-1.768089e-08	7.84334e-08	6.911824e-07
Median	8.2462e-05	-1.40724e-05	-2.193322e-05	7.459752e-05
RMS	0.001323703	0.001314568	0.001312277	0.001290693
Std Deviation	0.001331289	0.001322101	0.001319797	0.001298089
Variance	1.77233e-06	1.74795e-06	1.741864e-06	1.685035e-06
Std Error	0.000141916	0.000140937	0.000140691	0.0001383767
Skewness	-0.44998933	-0.30256637	-0.3352318	-0.4474666
Kurtosis	-0.03699146	-0.1832551	-0.15440891	-0.04787101

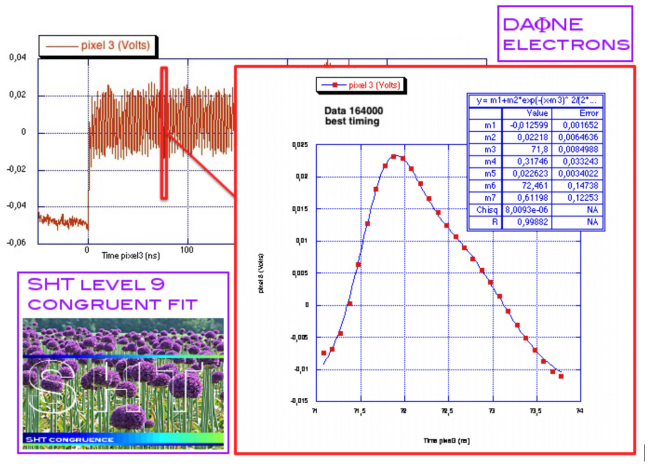

FIG. 19. SHT level 9 regression with a double Gaussian on a typical IR synchrotron radiation (pixel 3) double emission profile ("main" and "delayed") of a bunch of DAΦNE electrons.

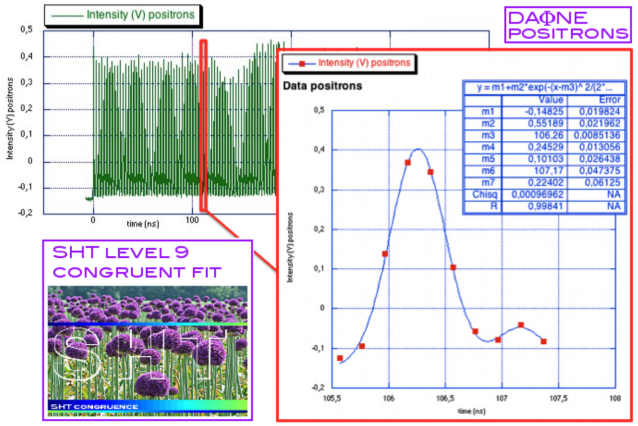

FIG. 21. SHT level 9 regression with a double Gaussian on a typical IR synchrotron radiation double emission profile ("main" and "delayed") of a bunch of DAΦNE positrons. Single photo-detector configuration.

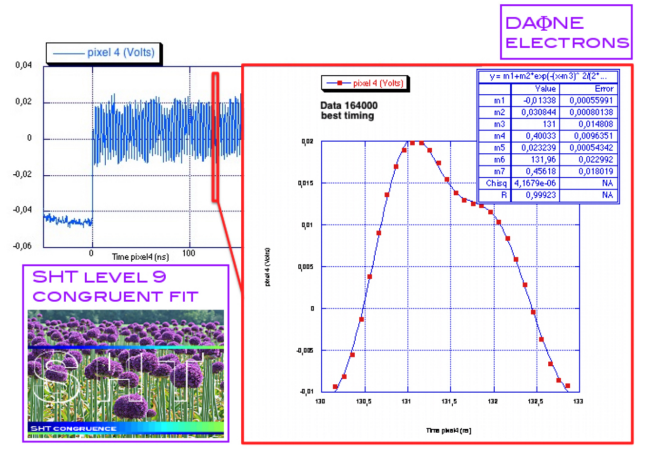

FIG. 20. SHT level 9 regression with a double Gaussian on a typical IR synchrotron radiation (pixel 4) double emission profile ("main" and "delayed") of a bunch of DAΦNE electrons.

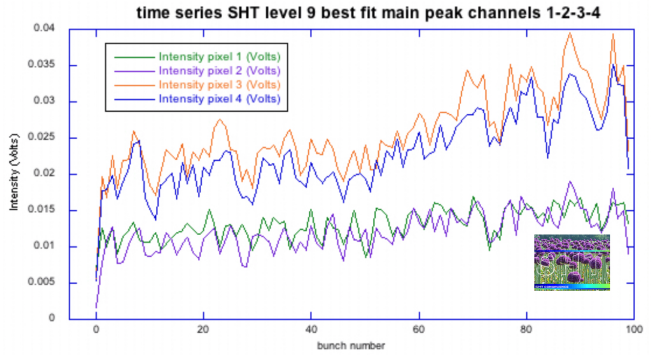

FIG. 22. Comparative and summary diagram of the 4 time series of the intensities (V) of the "main peaks" of IR synchrotron radiation emission of each bunch acquired by the MCT (pixel) 1-2-3-4 photo-detectors and ordered in the sequence of 100 bunches of a complete DAΦNE electron filling.

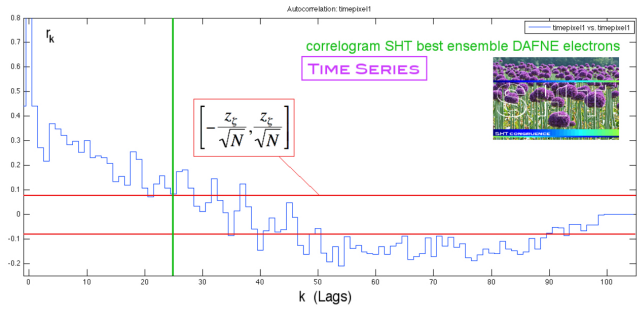

FIG. 23. Correlogram (main peaks) of a best ensemble Z^e. Confidence bands are highlighted in red. The marker ("boundary-lag") is marked in green at T / 4 (DAΦNE electrons).

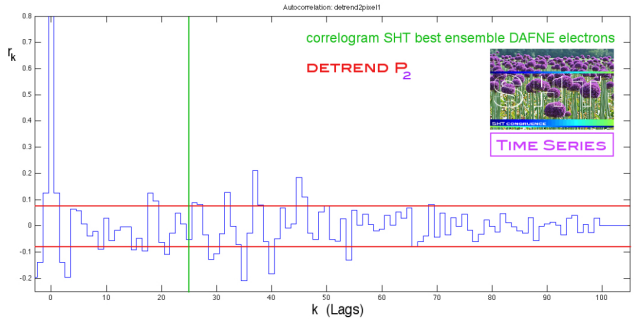

FIG. 24. Correlogram of the residues of the Z_t series (detrend P2 (t)) DAΦNE electrons.

XI. DICHOTOMY IN THE TIME-DOMAIN SR: DISCUSSION AND HYPOTHESIS.

At the end of this long analysis path, I discuss the evidence of the two contributions ("main" and "delayed") found and resolved in the time-domain synchrotron radiation emission signal. I called this evidence "dichotomy" in the time-domain SR.

From the previous chapters, it was clear that, neglecting the term "delayed", inevitable systematic errors are introduced which invalidate all the results of the analysis. I will also return to this point.

Obviously, the first thing I asked myself is if the dichotomy was caused by systematic effects introduced by the machine and / or by the experimental arrangement. But the results of the analysis of the time series exclude that the systematic contributions can alter in any way can the dominant trend component of the signal, which represents the deterministic evolution of the phenomenon in question.

Finally, I had confirmation of the existence of the delayed contribution in all other measurements performed with different sources and provisions and different MCT detectors (See the following table 4). In order not to weigh down this work, here I produce only the results of table 5.

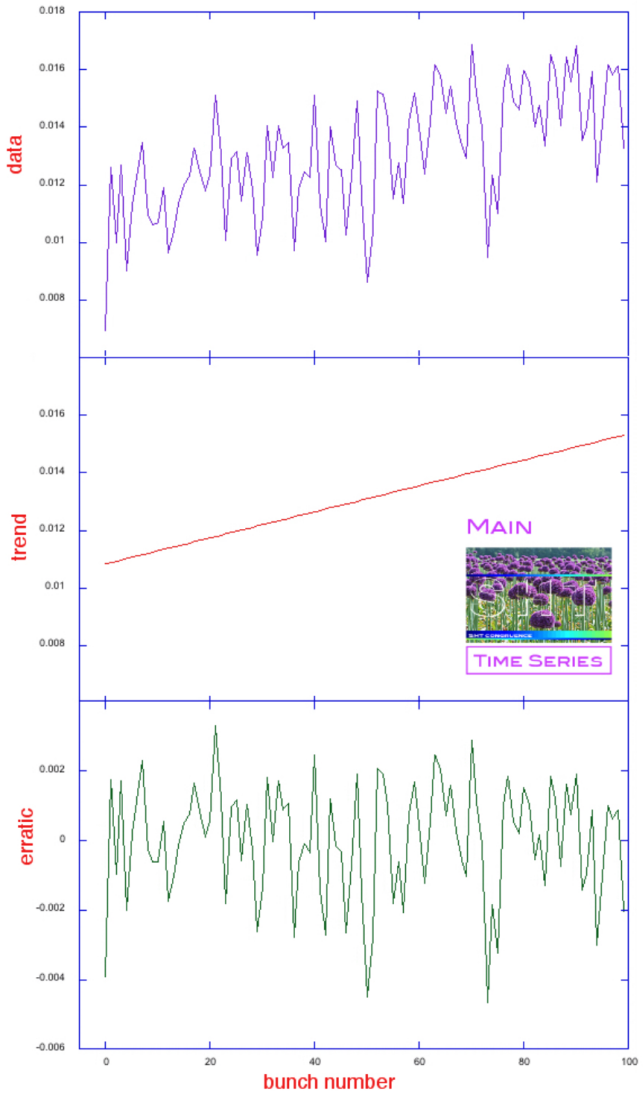

FIG. 25. Comparative and summary diagram of the decomposition of the Z_t series (main component - DAΦNE electrons)

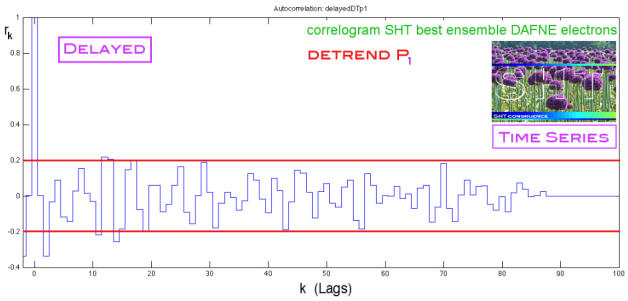

FIG. 26. Correlogram of the residues of the Z_t series (detrend P1 (t)). Delayed component - DAΦNE electrons.

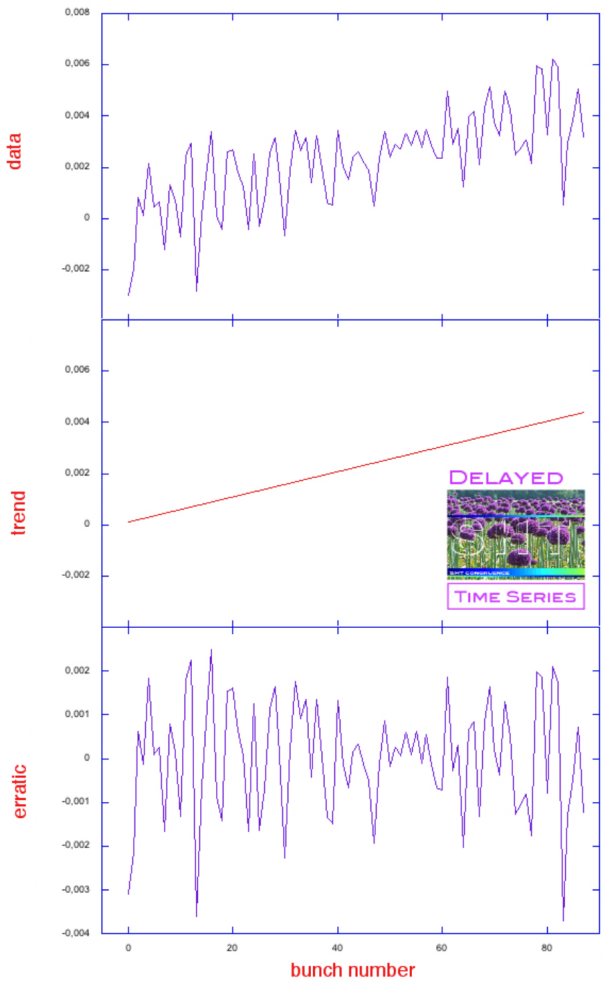

FIG. 27. Comparative and summary diagram of the decomposition of the Z_t series ("delayed" component - DAΦNE electrons)

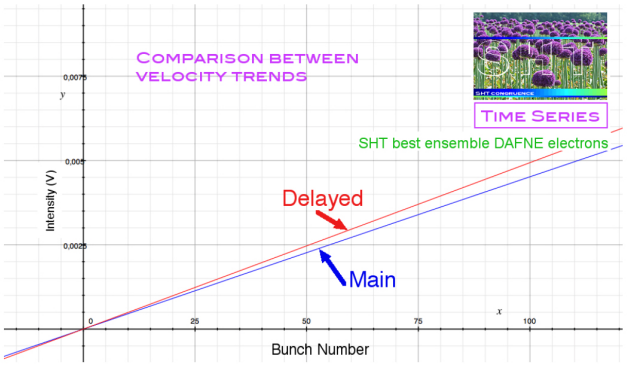

FIG. 28. Comparison between the trend models: "main" component vs "delayed". DAΦNE electrons.

TABLE IV. Time differences between the "main" and "delayed" components observed with different arrangements and / or sources.

Source and arrangement	Δt (ps)
Multi bunch DAΦNE electrons MCT array (pixel 1)	850 ±50
Multi bunch DAΦNE electrons MCT array (pixel 2)	1370 ±30
Multi bunch DAΦNE electrons MCT array (pixel 3)	700 ±200
Multi bunch DAΦNE electrons MCT array (pixel 4)	960 ±40
Multi bunch DAΦNE positrons MCT single channel	910 ±60
Multi bunch DAΦNE positrons MCT single channel	800 ±30
Multi bunch DAΦNE electrons MCT single channel	780 ±80
STREAK CAMERA DAΦNE positrons	64 ±6
Multi bunch HEFEI electrons MCT single channel	330 ±20

As an example, in the following figure 29 and table 5, I show the discrepancies obtained from the interpolations of the data by DAΦNE positron SR recorded at Frascati with a streak camera. The figure 29 shows the single profile regression (black curve, courtesy of Mikhail Zobov, Frascati National Laboratories) with the multiple regression (red curve) produced by SHT without neglecting the "delayed" component.

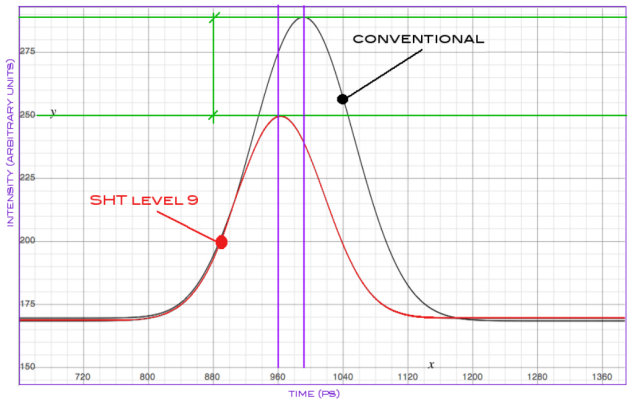

FIG. 29. DAΦNE positrons. Cartesian representation of the discrepancies between "conventional" interpolation (courtesy of M. Zobov, Frascati National Laboratories) and SHT level 9. As can be seen, "conventional" interpolation leads to an overestimation of both intensity, center and width. Neglecting the contribution of the delayed component therefore leads to a significant systematic error.

TABLE V. Streak Camera. DAΦNE positron SR. Systematic errors.

Δ (conventional vs SHT)	Discrepancies	Discrepancy percentages
$\Delta\sigma$	(8 ± 1) ps	15%
Δ(FWHM)	(18 ± 3) ps	14%
Δ(peak)	(28 ± 4) ps	3%
Δ(intensity)	(39 ± 7) a.u.	16%

XII. SR JOKES AT THE SPEED OF LIGHT.

The generally accepted theory on synchrotron radiation emission (See A. Hofmann [13]) is based on the hypothesis of the rigidity of the bunch of relativistic particles. The accelerated motion of the bunch in the field of a bending magnet is thus represented as the motion of a massive "super-particle", that emits radiation propagating in the vacuum (along a line of light) starting from a well-defined K opening (See the following figure 30).

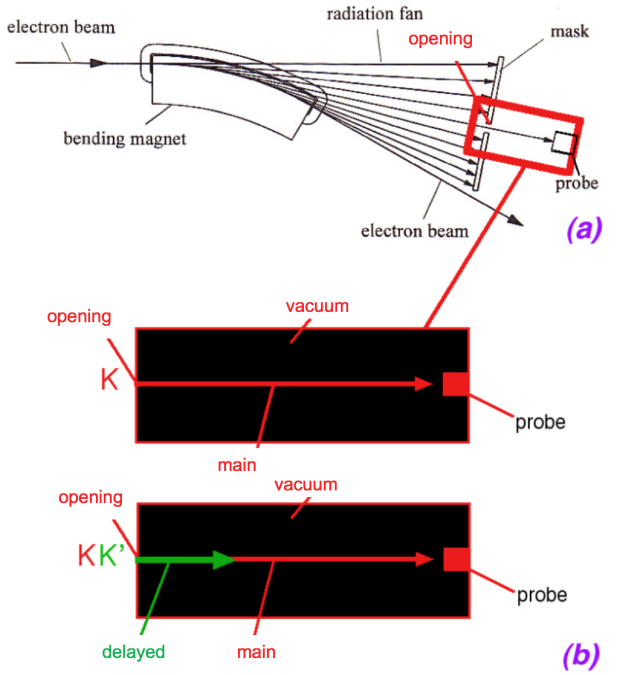

FIG. 30. (a) SR emission by an electron (positron) beam during accelerated motion in a bending magnet.
(b) Scheme of the emission of two light signals ("main" and "delayed") from the same source (opening) K. (Schematics modified after A. Hofmann [13])

I just know the length of the optical path in the case of Frascati and Hefei, as in the following table 6.

TABLE VI. Facility optical path lenght (courtesy of Frascati National Laboratory and Hefei Light Source, People's Republic of China)

Facility	Optical path lenght (m)
DAΦNE	25 ± 1
HEFEI	5 ± 1

So, in the next figure 31 and table 7, I calculated the percentage discrepancies $\Delta c/c$ in the case of DAΦNE, recalling the previous table 4

Now, as a possible explanation of this anomaly, I will focus on the structure of a bunch of particles.

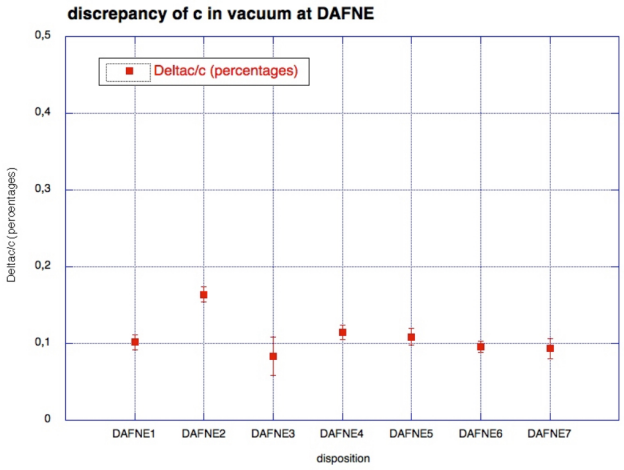

FIG. 31. Discrepancies $\Delta c/c$ in the case of DAΦNE (electrons).

TABLE VII. Percentage discrepancies $\Delta c/c$ in the case of DAΦNE (electrons).

Arrangement (DAΦNE electrons)	$\Delta c/c$ (%)
DAΦNE 1	0.10 ± 0.01
DAΦNE 2	0.163 ± 0.01
DAΦNE 3	0.08 ± 0.03
DAΦNE 4	0.114 ± 0.01
DAΦNE 5	0.11 ± 0.01
DAΦNE 6	0.095 ± 0.008
DAΦNE 7	0.09 ± 0.01

So let's start from the distribution of N electrons in a circular machine [22] .

$\rho_n(r,t) = e\frac{\delta(\rho-R)}{R}\delta(z)\frac{e^{in\varphi}}{2\pi}\sum_{k=1}^{N}e^{-in\varphi_k}$

where R is the radius of the machine. I am interested in the case where electrons are not evenly distributed in the machine. In this case, I will have a coherent radiation term (CSR) added to an incoherent radiation term (ISR), due to the individual contribution of each electron. To calculate the average power emitted by N electrons, I will have to mediate on all the angular positions of each particle included in the interval (-$\alpha/2$, $\alpha/2$) as follows

$\overline{\left|\sum_{k=1}^{N}e^{-in\varphi_k}\right|^2} = N + N(N-1)\left[\frac{1}{\alpha}\int_{-\alpha/2}^{\alpha/2}d\varphi\cos n\varphi\right]^2 = N + N(N-1)\left[\frac{\sin n\alpha/2}{n\alpha/2}\right]^2$

Where I can distinguish the terms of ISR$\sim$N and CSR$\sim$N^2 and calculate the total power of the coherent radiation emitted by N electrons, as follows

$P_{CSR}^{(N)} = N^2\sum_{n=1}^{\infty}\left[\frac{\sin n\alpha/2}{n\alpha/2}\right]^2 P_n$ With N$\gg$1

Now, since the number N of particles in an accumulation ring is very large (for DAΦNE we have typical values of the order of 10^{10} - 10^{11} particles / bunch), the intensity of the CSR could be not negligible. I therefore consider the spectrum of radiated power, as follows [23–27]

$\frac{dP}{d\lambda} = \frac{dp}{d\lambda}\left[N(1-g(\lambda)) + N^2 g(\lambda)\right]$

where λ is the wavelength of the radiation, p the power emitted by a single particle, N is the number of particles per bunch and g the so-called "CSR form factor", given by the following equation

$g(\lambda) = \left| \int_{-\infty}^{+\infty} n(z)\, e^{2\pi i \cos(\theta) z/\lambda} dz \right|^2$

where $0 \leq g \leq 1$, n(z) is the bunch normalized distribution and θ is the angle between the longitudinal direction z and the observation point. For $\theta = 0$ the form factor g (λ) is precisely the square of the Fourier transform of the bunch distribution. In this case, to define $dp/d\lambda$ I took into consideration the effect of the vacuum chamber screen, hence the cut-off wavelength is

$\lambda_0 \approx 2h\sqrt{\frac{h}{\rho}}$

where h is the total height of the vacuum chamber and ρ the radius of curvature of the trajectory of the particle. Ultimately, to have a significant CSR contribution, we must have:

$\begin{cases} g(\lambda) > \frac{1}{N-1} \sim \frac{1}{N} \\ \lambda < \lambda_0 \end{cases}$

As an example, in our case, we evaluate the form factor for Gaussian bunches. For $\theta = 0$ I have:

$\frac{2\pi\sigma_z}{\sqrt{\ln(N)}} < \lambda < \lambda_0 = 2h\sqrt{\frac{h}{\rho}}$

where σ_z is the bunch lenght. From here, I see well that to have CSR emission it is necessary to have "short" bunches with large cut-off wavelengths. In the case of "real" machines, the CSR contribution can be observed in the typical frequency range of THz.

XIII. THE MODEL OF THE COHERENT FRACTAL NEMATIC MESOPHASE (CFNM).

At this point, I want to introduce a model based on some considerations of statistical mechanics of complex and disordered systems [28–38]. It will help me to explain both the evidence of a delayed component in the synchrotron radiation profile of each bunch and the reason why I considered the contribution of coherent radiation (CSR).

I begin with the general density operator

$n(\overrightarrow{r}) = \sum_\alpha \delta(\overrightarrow{r} - \overrightarrow{r}_\alpha) \rightarrow \langle n(\overrightarrow{r}) \rangle$

and with the two-point density correlation function

$C_{nn}(\overrightarrow{r}_1, \overrightarrow{r}_2) = \langle n(\overrightarrow{r}_1)\ n(\overrightarrow{r}_2) \rangle$

from which I define the pair distribution function

$g(\overrightarrow{r}_1, \overrightarrow{r}_2)$

such that:

$\langle n(\overrightarrow{r}_1) \rangle\, g(\overrightarrow{r}_1, \overrightarrow{r}_2)\, \langle n(\overrightarrow{r}_2) \rangle = \left\langle \sum_{\alpha \neq \alpha'} \delta(\overrightarrow{r}_1 - \overrightarrow{r}_\alpha)\, \delta(\overrightarrow{r}_1 - \overrightarrow{r}_{\alpha'}) \right\rangle$

in the present case, fixed a time $\tau > 0$, consider a distribution of clusters of particles having the topological qualities of "micro-bunches" of σ_z length with a density given by

$n(\sigma_z) = \sum_\alpha \delta(\sigma_z - \sigma_z^\alpha) \rightarrow \langle n(\sigma_z) \rangle$

where the range of scale variation is given by the following interval

$\Lambda < \sigma_z < R_s$

where Λ and R_s represent, respectively, the lower and upper cut-off scales. At this point, I assume that the observed anomaly is the result of a collective behavior of the particles inside the bunch, which generates a macroscopic coherence effect. Then, our lower and upper cut-off scales, Λ and R_s , will both depend on the cut-off wavelength of the Schwinger model [22] , which I recall below

$\lambda_0 \approx 2h\sqrt{\frac{h}{\rho}}$

where h is the total height of the vacuum chamber and ρ the radius of curvature of the "cluster" trajectory: that is, R_s is the maximum cluster size and can be identified with the length of the bunch intended as "rigid system" or "super-particle". Ultimately, there will be a cluster of particles that will emit synchrotron radiation along the direction of motion. The physical model that best describes this effect is that of the nematic mesophase of a liquid crystal (See PG de Gennes, FC Frank and S. Chandrasekhar [39–42]). Coherence can therefore be explained by the variation of the average density as a function of the bunch dimension σ_z in the scale range given by the above interval (Λ,R_s), as the following:

$\lim_{\sigma_z \rightarrow \infty} \langle n(\sigma_z) \rangle \sim \lim_{\sigma_z \rightarrow R_s} \langle n(\sigma_z) \rangle \sim \sigma_z^{D_H}$

With

$D_H \geq D_T$

Where D_H is the *Hausdorff dimension* and D_T the topological dimension.

Therefore, we have a "super-bunch" made by a nematic fractal mesophase of particle micro-bunches emitting IR-SR along the direction of motion, according to the snapshot the following figure 32

As can be seen from the snapshot of the simulation of the previous figure 32, a contribution of coherent radiation emission (CSR) can occur as soon as the micro-bunches reach the scale

$\sigma_z \sim \lambda_0$

Consider therefore

$N = n(\sigma_z)_{\sigma_z > \lambda_0} + n(\sigma_z)_{\sigma_z < \lambda_0}$

Where N is the total number of particles, an appreciable contribution of coherent emission will be expressed by the following

$\frac{dP}{d\lambda} = \frac{dp}{d\lambda} \left[N(1 - g(\lambda)) + N^2 g(\lambda) \right]$

Where the form factor will depend on N as

$g(\lambda) > \frac{1}{N-1} \sim \frac{1}{N}$

With $\lambda < \lambda_0$

The observed anomaly in IR-SR waveforms can thus be explained by the micro-bunch emission when $\sigma_z \precapprox \lambda_0$.

XIV. A WIDER CONCEPT OF STIFFNESS

Going further, we generated a simulation for the SR emission during the motion of the Fractal Nematic Mesophase in a DAΦNE bending magnet, considering that each "super-bunch" is separated by the average time interval of 2.7 ns (See the next figure 33).

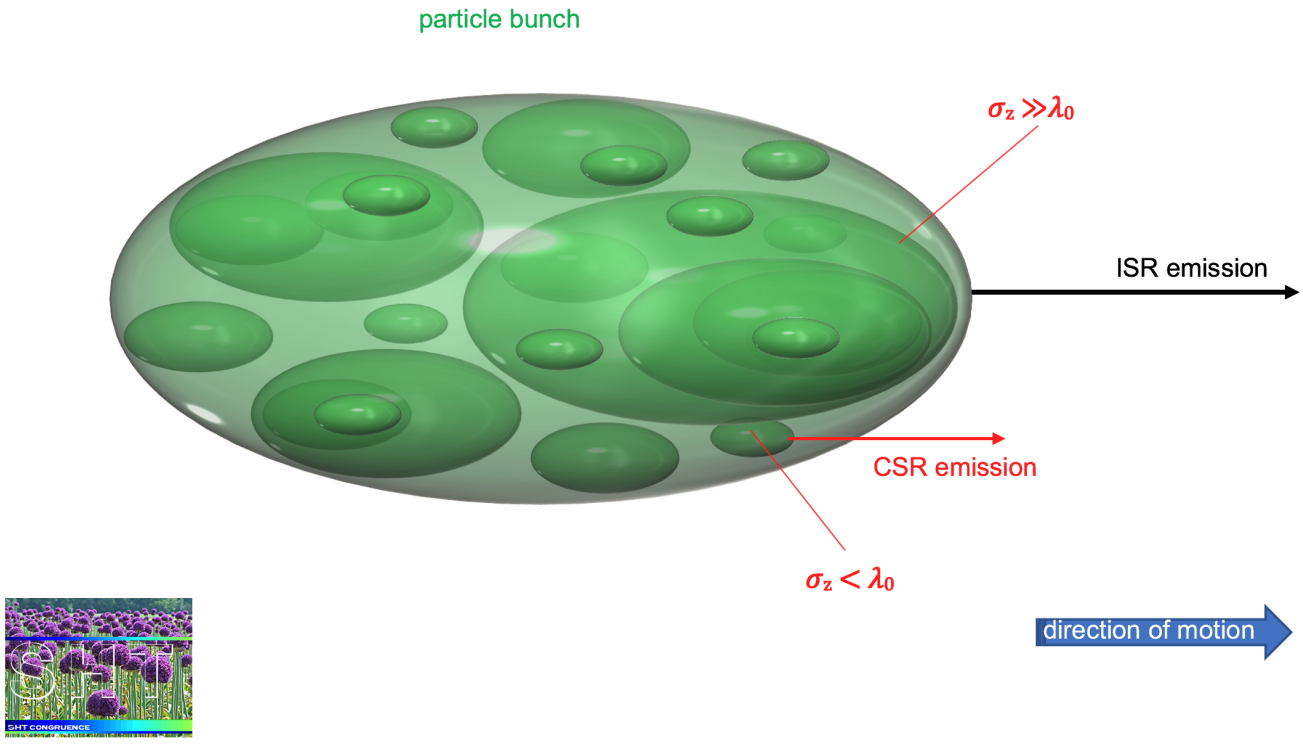

FIG. 32. Fractal Nematic Mesophase. Snapshot of a SHT simulation

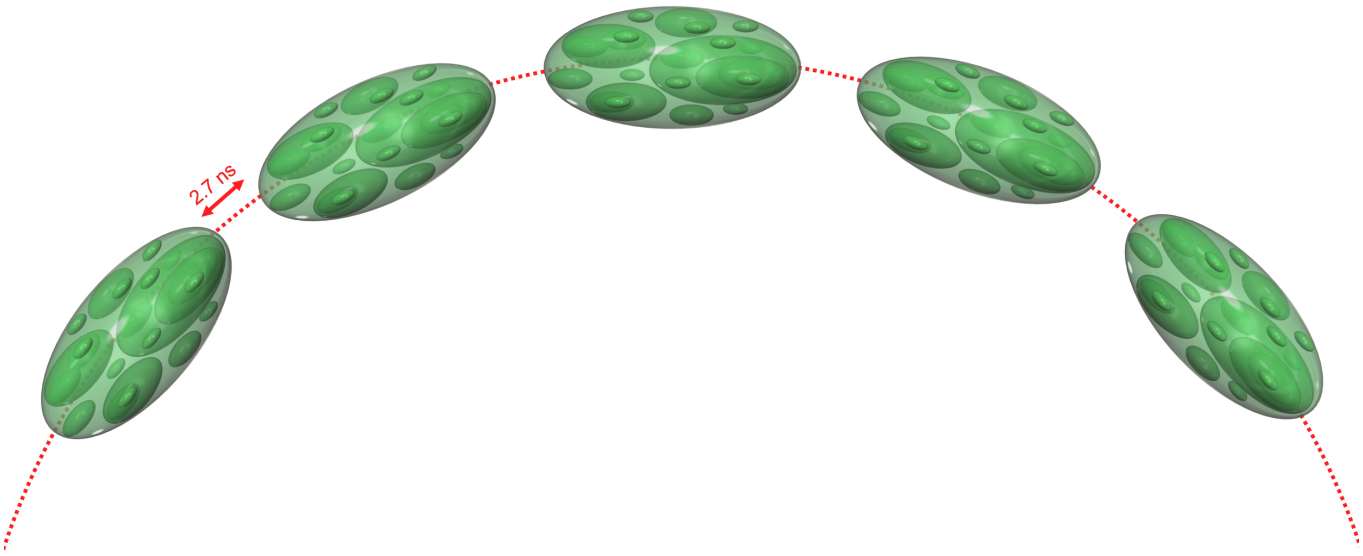

FIG. 33. Motion of a "fractal nematic mesophase" of particles in a DAΦNE bending magnet.

This simulation gives us the opportunity to generalize Schwinger's "rigid bunch" concept using liquid crystal theory.

In the non relativistic case, the *Stiffness* for the Nematic Phase is a four rank tensor K_{ijkl}, such that we have the free energy

$F_{el} = \frac{1}{2} \int d^d x \; K_{ijkl} \nabla_i n_j \nabla_k n_l$

The free energy must be invariant under uniform rotations of the whole bunch and under the symmetry operations $\overrightarrow{n} \rightarrow -\overrightarrow{n}$ and $\overrightarrow{x} \rightarrow -\overrightarrow{x}$ where $\overrightarrow{n}$ is a unit vector. This is a first interesting clarification, where we pass from an isotropic state of distribution of the particles, to a "condensed" state of lower symmetry, which is precisely the nematic phase [43] . This will help us in the future when it comes to building models for beam diagnostics. The above considerations imply that the stiffness tensor has three independent components, given by the elastic constants K_1, K_2, K_3 . We come then to an elastic energy for the nematic phase, the so-called "Frank's free energy" [42] . In the non-relativistic case, we will have that:

$$F_n = \frac{1}{2} \int d^d x \left\{ K_1 \left(\overrightarrow{\nabla} \cdot \overrightarrow{n} \right)^2 + K_2 \left[\overrightarrow{n} \cdot \left(\overrightarrow{\nabla} \times \overrightarrow{n} \right) \right]^2 + K_3 \left[\overrightarrow{n} \times \left(\overrightarrow{\nabla} \times \overrightarrow{n} \right) \right]^2 \right\} \quad (11)$$

Ignoring for now the distortions of "splay" and "twist", we have a formula (non relativistic) for the free energy of our system subjected to bending only.

We then have:

$$F_n \cong \frac{1}{2} \int d^d x \left\{ K_3 \left[\overrightarrow{n} \times \left(\overrightarrow{\nabla} \times \overrightarrow{n} \right) \right]^2 \right\}$$

Since the transposition in relativistic form requires considerable time and space, for now we omit it. As a starting point, however, we want to mention the dimensional issue because it will be very useful in the future. In the non relativistic form, the elastic constant K_3 has units of energy/lenght of order $k_B T_{NI}/a$, where T_{NI} is the isotropic-to-nematic transition temperature and a is a typical molecular length. In our case, we can keep the dimensional quantities, as long as we introduce the bunch lenght σ_z . It would be interesting to start from here to derive Frank's free energy in the relativistic case, but space requirements require us to close this work here.

XV. CONCLUSIONS

Diagnostics represents a complex of activities and techniques, vital for the operation of an accelerator machine, which offers indispensable support both for high energy physics experiments and for the use of the emission of synchrotron radiation in a parasitic or dedicated way .

This paper presents and discusses the results of an unconventional statistical analysis from the experimental data recovered from an experiment of the National Institute of Nuclear Physics called "3 + L". The experiment consisted in the study of the bunch-by-bunch and turn-by-turn IR synchrotron radiation emission by electrons and positrons of the Φ-DAΦNE Factory, collected by uncooled ultrafast photo-detectors based on HgCdTe (MCT) hetero-structures. The analysis also considered data collected at the Hefei Light Source (HFL) of the National Synchrotron Radiation Laboratory (NSRL) of the People's Republic of China.

MCT systems represent valid and competitive elements, possibly capable of replacing - or in any case supporting - the "streak cameras".

A useful application of this analysis consists in the generation of space-time maps according to the topology on the detector matrix. This result can lead to the development of a future real time imaging.

The analysis clearly showed the unexpected presence of an "anomaly" in the waveform of the IR synchrotron radiation emission in the time domain of each single bunch of electrons and positrons. This "anomaly" is resolved, in the temporal domain, in two distinct terms, one of which is "delayed" by a few hundred of ps with respect to the other. Of course, I immediately thought that this anomaly was a systematic error of the measuring apparatus. Checks on the data and on the measuring device excluded this possibility. The measurement was in fact repeated both with changes of the conditions and hardware of the local apparatus (including the detectors) and with a change of the facility (Hefei). In all these cases, the measurement has always shown the same "anomaly".

I conclude by saying that the MCT detectors were able (thanks to the SHT analysis) to follow the longitudinal dynamics, as well as to identify, monitor and characterize the beam instability, which we called "anomaly", consisting in the presence of a "delayed" term in the SR emission of each bunch. So this was certainly a positive result of this long work.

To explain the observed anomaly, we considered Schwinger's "rigid bunch" model as incorrect. We thus proposed a model called "CFNM" (Coherent Fractal Nematic Mesophase), based on considerations of statistical mechanics of complex systems about the properties of density and coherence of the bunch of particles, exploiting an analogy with the nematic mesophase of a liquid crystal.

This could lead to significant consequences in the study, modeling and measurement of the operating parameters of future accelerator machines and colliders especially with regard to emittance and brightness.

XVI. ACKNOWLEDGMENTS

Frascati National Laboratories (LNF)
Sapienza University of Rome
National Institute for Nuclear Physics (INFN)
HFL (Hefei Light Source) at the National Synchrotron Radiation Laboratory (NSRL) of the People's Republic of China
VIGO System SA
Also, for the valuable advices and passionate discussions, I would like to thank, among others
Prof. Nicola Cabibbo (1935-2010)

Prof. Luciano Maiani
Prof. Giorgio Parisi
Prof. Sheldon Lee Glashow
Prof. Roberto Coisson
Prof. Giuseppe Diambrini Palazzi

Dr. Pantaleo Raimondi
Dr. Alessandro Drago
Dr. Catia Milardi
Dr. Mikhail Zobov

---

[1] K. Wille, The Physics of Particle Accelerators (Oxford University Press, 2001).

[2] C. C. A. School) and CERN, Genève, Switzerland, Beam Diagnostics, in *CAS (Cern Accelerator School), Dourdan France 28 May-6 June 2008, Dourdan France; Geneva* (2008).

[3] Stanford University, Stanford, California 94305, USA, SLAC National Accelerator Laboratory.

[4] High Energy Accelerator Research Organization (KEK).

[5] A. Bocci *et al.*, The Time Resolved Positron Light Emission (3+L) experiment: a novel diagnostic tool for the DAΦNE positron ring. LNF–09/15 (2009).

[6] M. C. Guidi, M. Piccinini, A. Marcelli, A. Nucara, E. Burattini, and P. Calvani, Optical performances of SINBAD, the Synchrotron INfrared Beamline At DAΦNE, Journal of the Optical Society of America A **22**, 2810 (2005).

[7] J. Piotrowski and A. Piotrowski, MCT Photo detectors.

[8] J. Piotrowski and A. Piotrowski, Proc. SPIE (2005) pp. 117–117.

[9] G. Z. del Balzo, Statistical Field Theory of the Conduction of Nerve Impulses, Theoretical Biology and Medical Modelling (2020).

[10] G. Z. del Balzo, Category calculus and applications. U.S. Copyright Office n. TXU001773372; SIAE-OLAF n. 9903198/1999; SIAE-OLAF n. 2011000210/2011; SIAE-OLAF n. 2011000489/2011 (1999-2011).

[11] H. Frauenfelder, Energy Landscape and Dynamics of Biomolecules, Journal of Biological Physics **31**, 413 (2005).

[12] H. Frauenfelder, , *et al.*, The energy landscapes and motions of proteins, Science **254**, 1598 (1991).

[13] A. Hofmann, The Physics of Synchrotron Radiation (Cambridge University Press, 2004).

[14] E. B. Dagum, *Analisi delle serie storiche* (Springer Verlag, 2002).

[15] G. Massarotto, Lezioni sull'analisi delle serie temporali.

[16] P. J. Brockwell, *Time Series: Theory and Methods*, edited by and others (Springer Verlag, 1991).

[17] W. M. Persons, Indices of Business Conditions, Review of Economic Statistics , 5 (1919).

[18] J. D. Hamilton, *Time Series Analysis*, edited by U. P. of CA (1994).

[19] For the sake of brevity, in this work, I have omitted to include the results of the error distribution in the various steps and levels of the SHT analysis, apart from the analysis of the time series, which are however available on request.

[20] The estimation of the different components of a time series is often difficult and risky especially because it concerns.

[21] In order not to weigh down the text, I omit the analysis of the correlograms of the residues with the respective graphs, which I reserve the right to produce separately, if of interest.

[22] J. Schwinger, On Radiation by Electrons in a Betatron (1945), in *A Quantum Legacy: Seminal Papers of Julian Schwinger*, edited by K. A. Milton *et al.* (World Scientific, 2000) p. 307.

[23] F. Sannibale, International Committee for Future Accelerators, *et al.*, Stable CSR in storage rings: a model, Beam Dynamics Newsletter n. 35 (2004).

[24] A. Abo-Bakr, Coeherent Emission of Synchrotron Radiation and Longitudinal Instabilities, Proceedings of the 2003 Particle Accelerator Conference ().

[25] A. Abo-Bakr, Bunch lenght measurements at Bessy, Proceedings of the 2003 Particle Accelerator Conference ().

[26] Abo-Bakr, . C. E. Al, G. H. Mayes, . F. Hoffstaetter, and A. Sannibale, Stable CSR in storage rings: a model" in Beam Dynamics Newsletter n. 35, International Committee for Future Accelerators, in *Proceedings of the 2003 Particle Accelerator Conference*, Vol. 17 (1946) pp. 6–6.

[27] C. Biscari, ed., *International Committee for Future Accelerators*, Vol. 35 (W. Chou, 2004).

[28] A. Gabrielli, F. Labini, M. Joyce, and L. Pietronero, Statistical Physics for Cosmic Structures (Springer, 2004).

[29] B. Mandelbrot, The Fractal Geometry of Nature (W.H Freeman and Company, 1982).

[30] P.-G. de Gennes and Collège de France, *Collection des principales œuvres de Pierre-Gilles de Gennes*, edited by and others (Collège de France, 2009).

[31] P. M. Chaikin and T. C. Lubensky, *Principles of condensed matter physics* (Cambridge University Press, 1995).

[32] T. Halsey and A. Mehta, *Challenge in Granular Physics* (World Scientific, 2002).

[33] A. Vulpiani *et al.*, *Chaos and Coarse Graining in Statistical Mechanics* (Cambridge University Press, 2008).

[34] R. Badii and A. Politi, *Complexity*, Cambridge Nonlinear Science Series (Cambridge University Press, 1997).

[35] R. Ball, V. Kolokoltsov, and R. S. Mackay, eds., *Complexity Science - The Warwick Master's Course*, London Mathematical Society Lecture Note Series (Cambridge University Press, 2013).

[36] R. Herrmann, *Fractional Calculus* (World Scientific, 2011).

[37] A. Vulpiani *et al.*, *Chaos*, series on Advances in Statistical Mechanics (World Scientific, 2010).

[38] D. P. Feldman, *Chaos and Fractals* (Oxford University Press, 2012).

[39] P. de Gennes, *Pierre-Gilles de Gennes' Works Collected By The*, edited by and others.

[40] P. de Gennes and J. Prost, *The Physics of Liquid Crystals* (Clarendon Press, Oxford, 1993).

[41] S. Chandrasekhar, *Liquid Crystals* (Cambridge University Press, 1992).

[42] F. C. Frank, Liquid Crystals. On the theory of liquid crystals, Discussion of the Faraday Society **25** (1958).

[43] L. O. Onsager, The Effects of Shape in the Interaction of Colloidal Particles, Ann . N.Y. Acad. Sci. **51** (1949).

Declarations:
I declare no competing interests

Figures

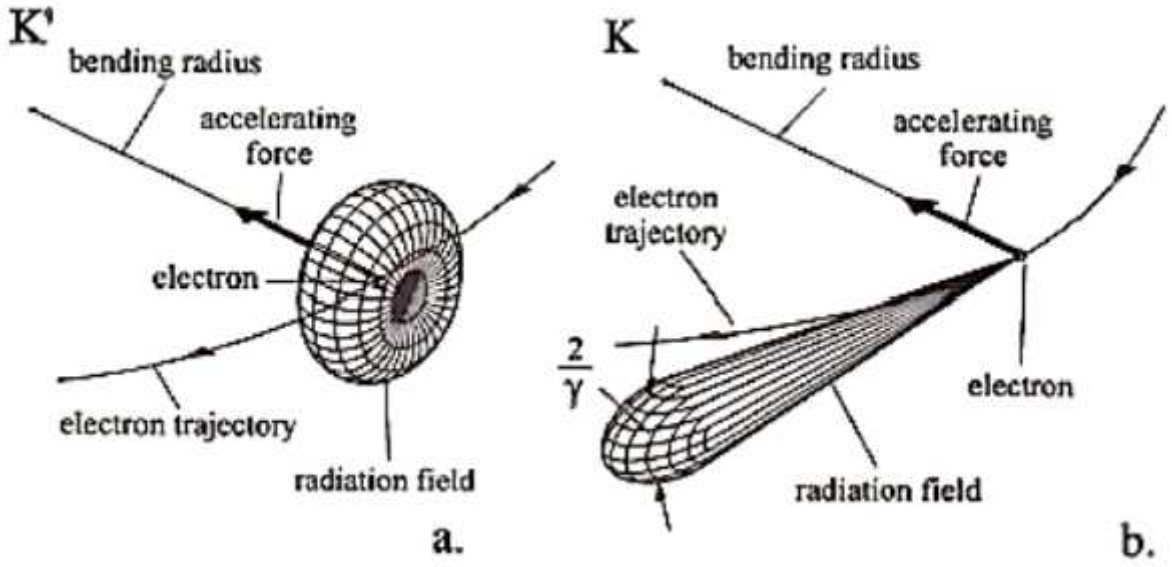

Figure 1

Distribution of the synchrotron radiation field in the center of mass system (a) and in the laboratory system (b). Note the very directional distribution, extended in a cone with an amplitude approximately equal to 1 / (b). Courtesy of K. Wille [1]

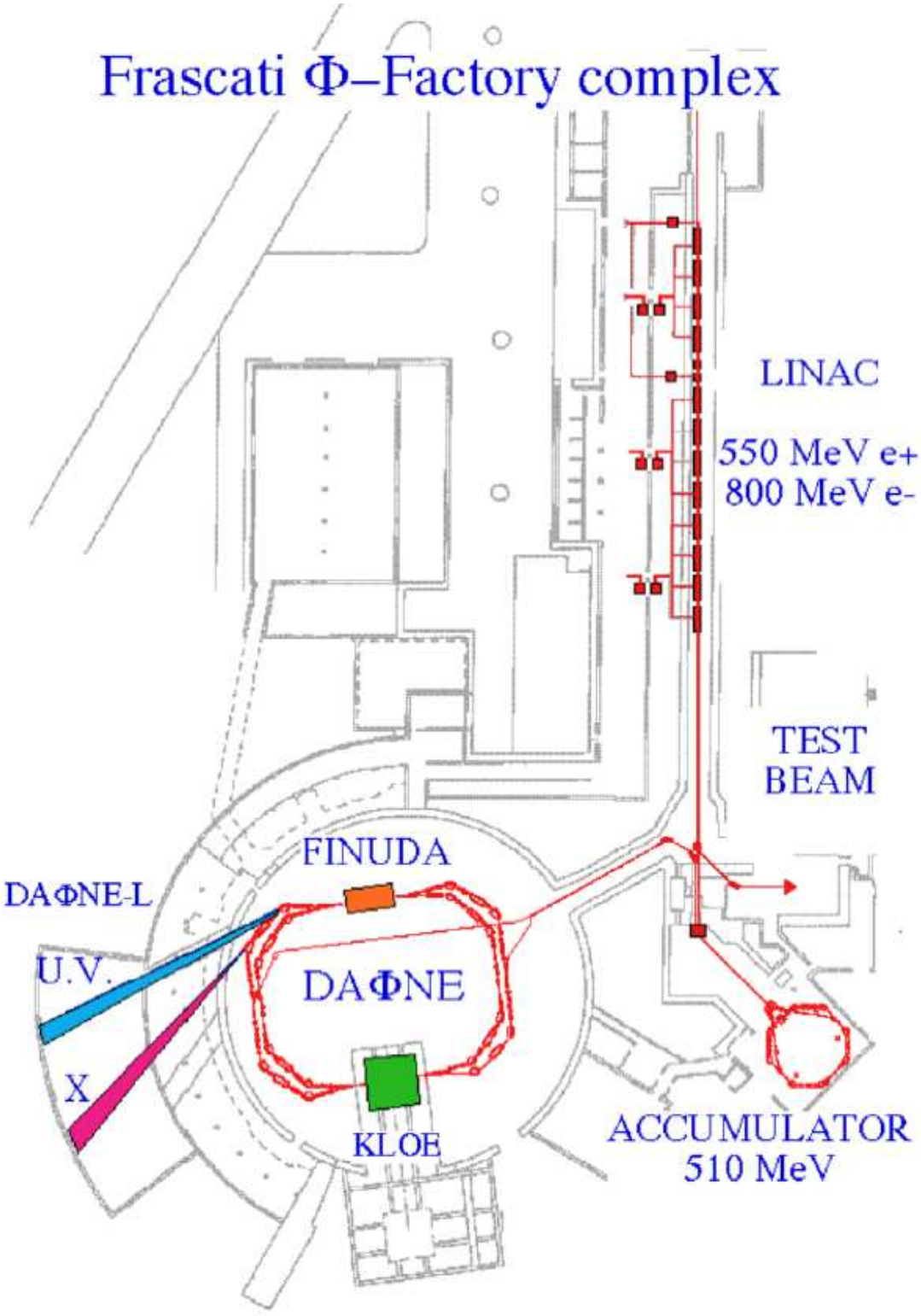

Figure 2

Schematic of DA□NE injection system (courtesy of Frascati National Laboratories).

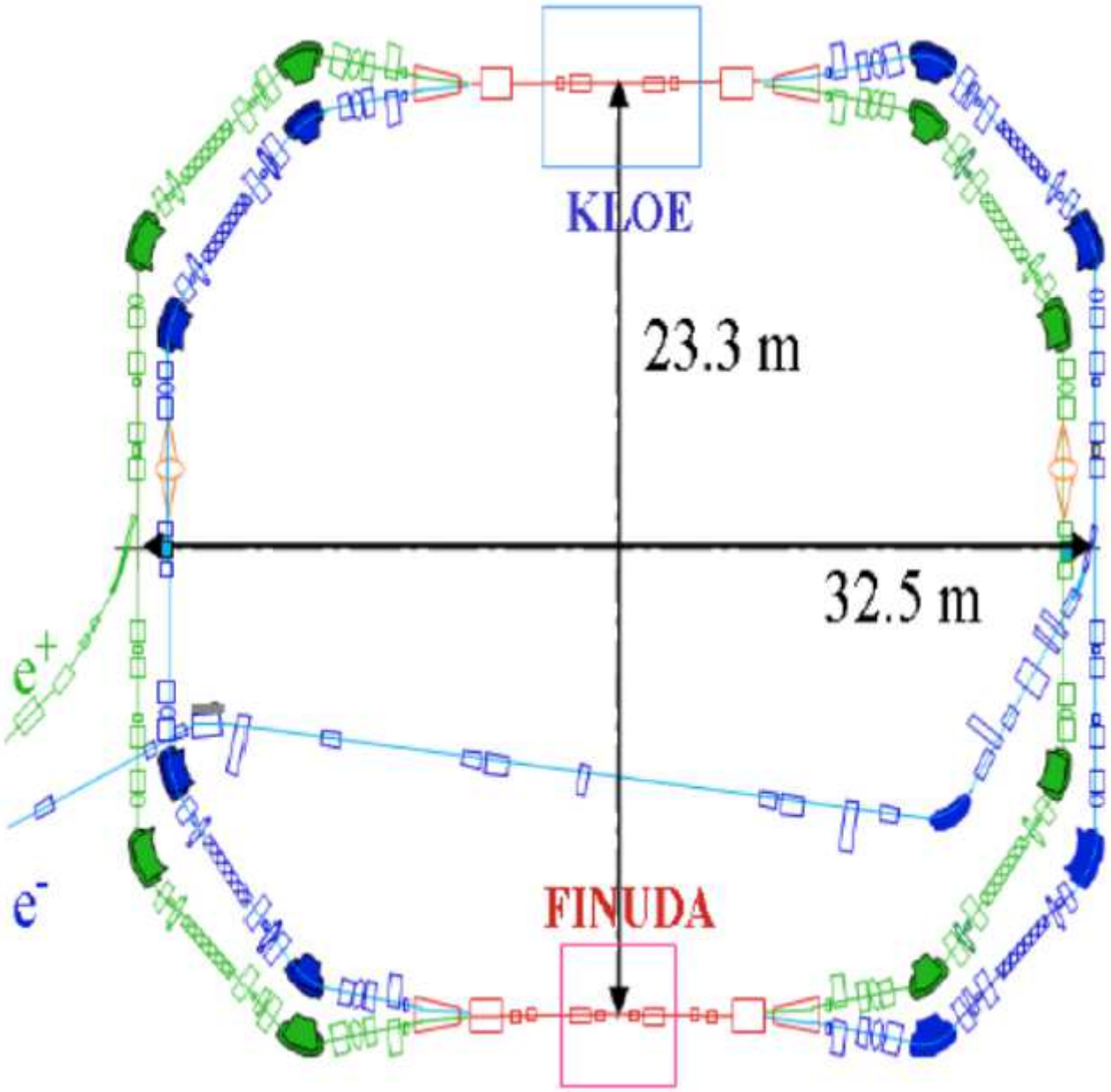

Figure 3

Schematic of the two main rings of DA□NE (courtesy of Frascati National Laboratories)

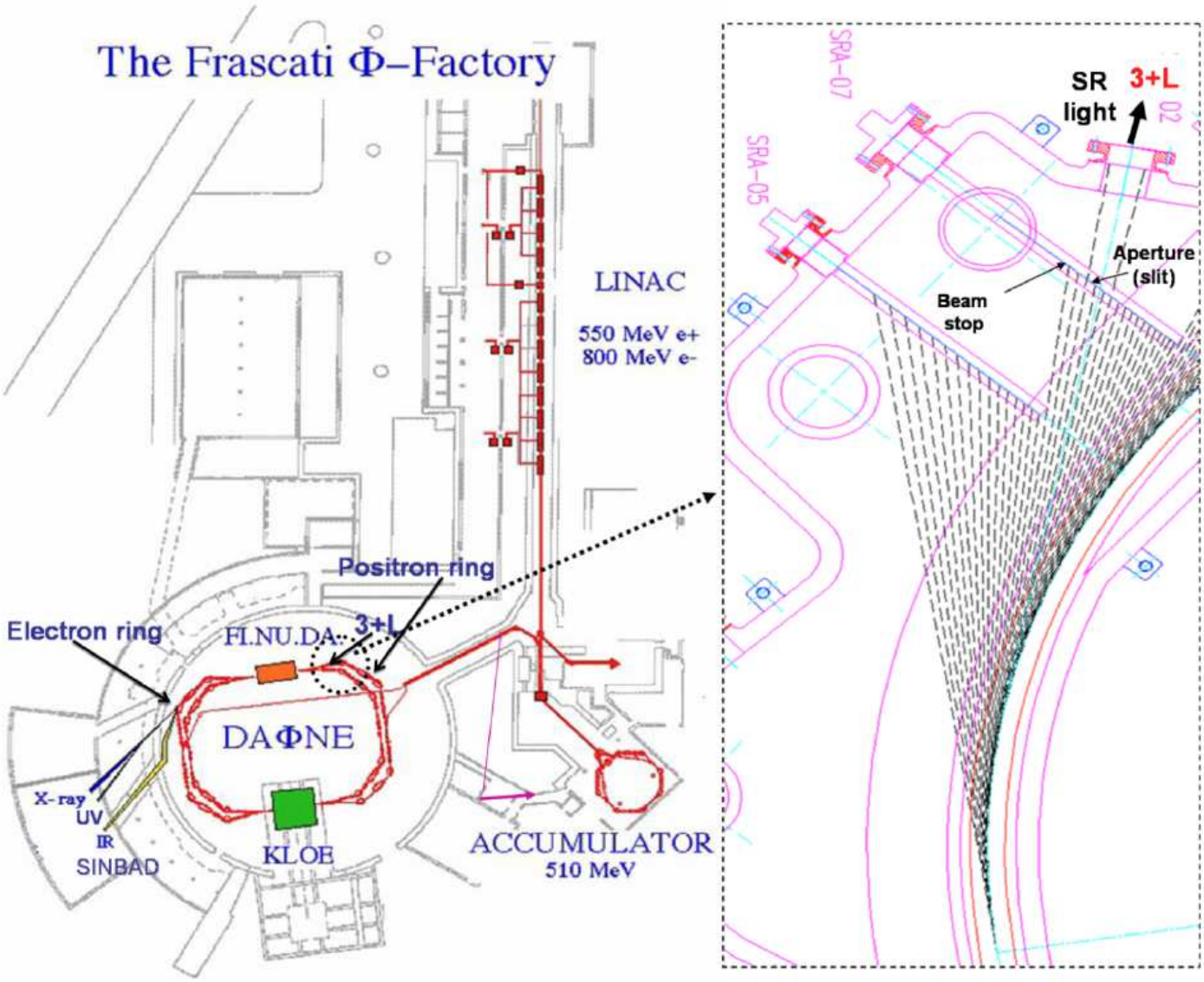

Figure 4

Layout and arrangement of experiment 3 + L at DA□NE (courtesy of Frascati National Laboratories)

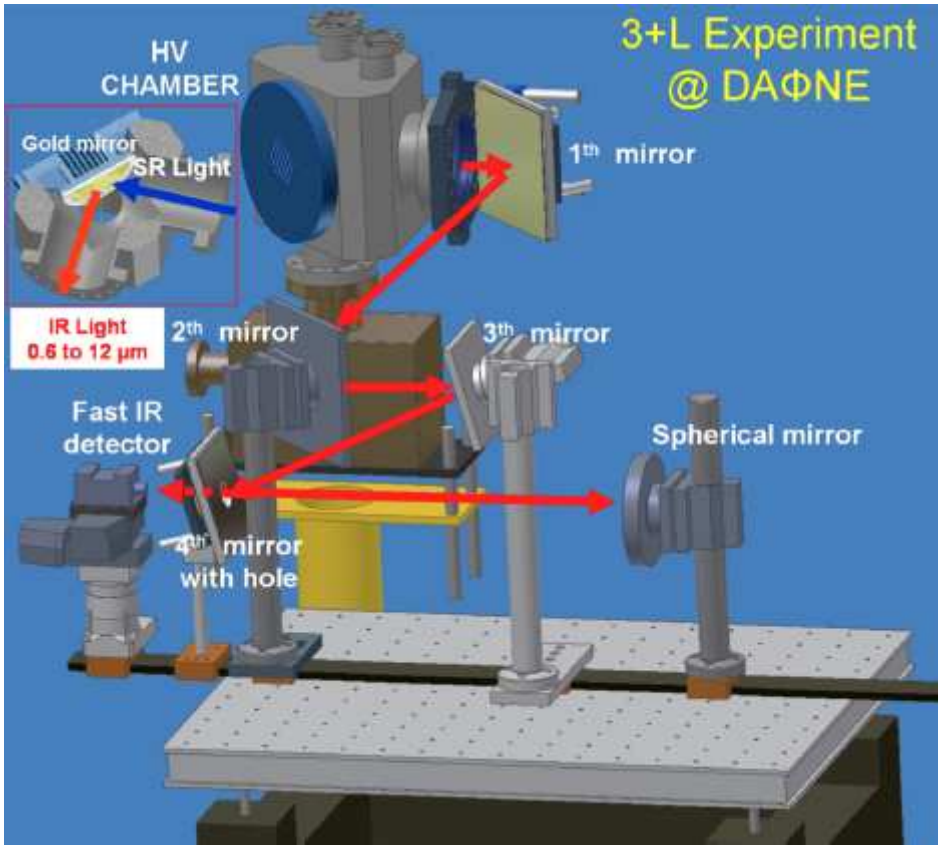

Figure 5

Optical layout of the experiment 3 + L with the "front end" structure, the optical table, the mirrors and the IR detector. The ideal path of IR radiation, from input to focusing optics is shown in red (courtesy of Frascati National Laboratories).

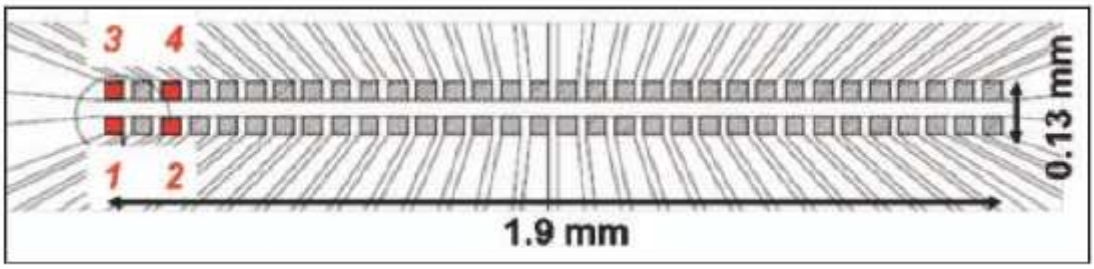

Figure 6

Matrix structure of MCT detectors with 4 activated channels (in red) (courtesy of Frascati National Laboratories and VIGO System SA [7])

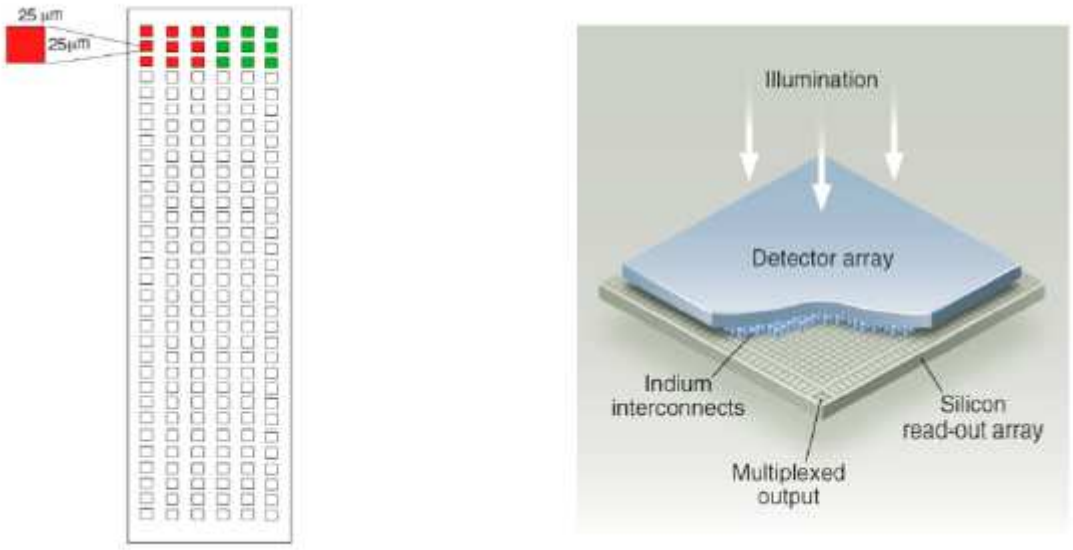

Figure 7

(Left) Optimized topology for a MCT detector matrix. (Right) Detector "anatomy" (courtesy of Frascati National Laboratories and VIGO system SA [7])

Figure 8

SHT category calculus logo

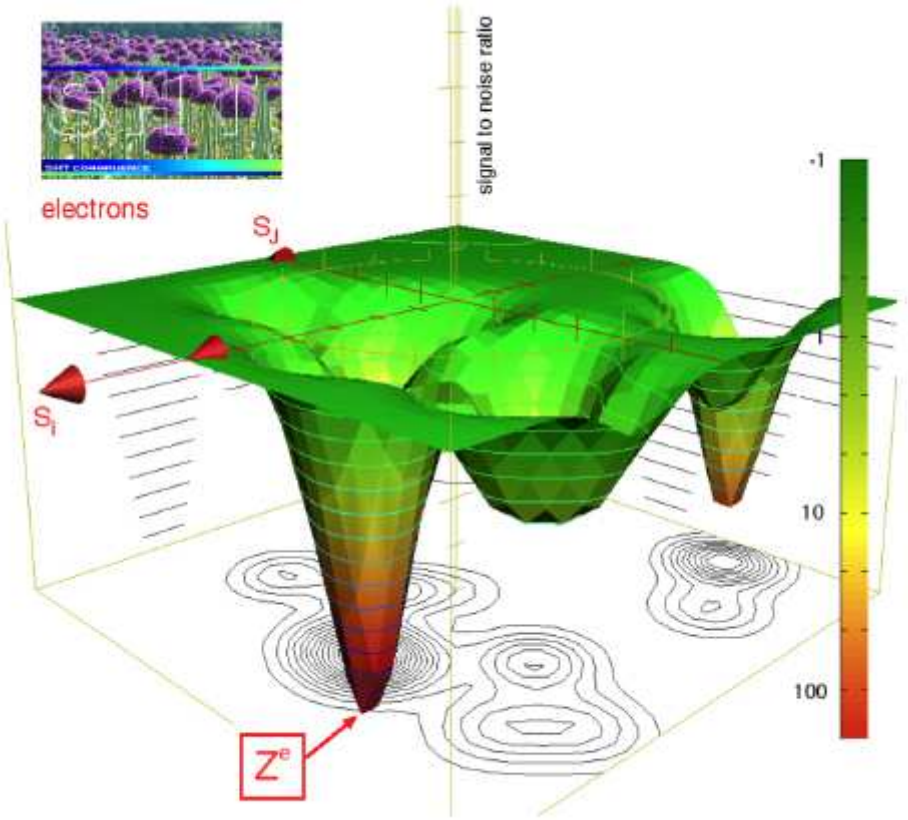

Figure 9

Level 1 - Data-Funnel of an ensemble of matrices relating to DA□NE electron synhcrotron radiation emission data. The absolute minimum Ze identifies the best values of the ensemble.

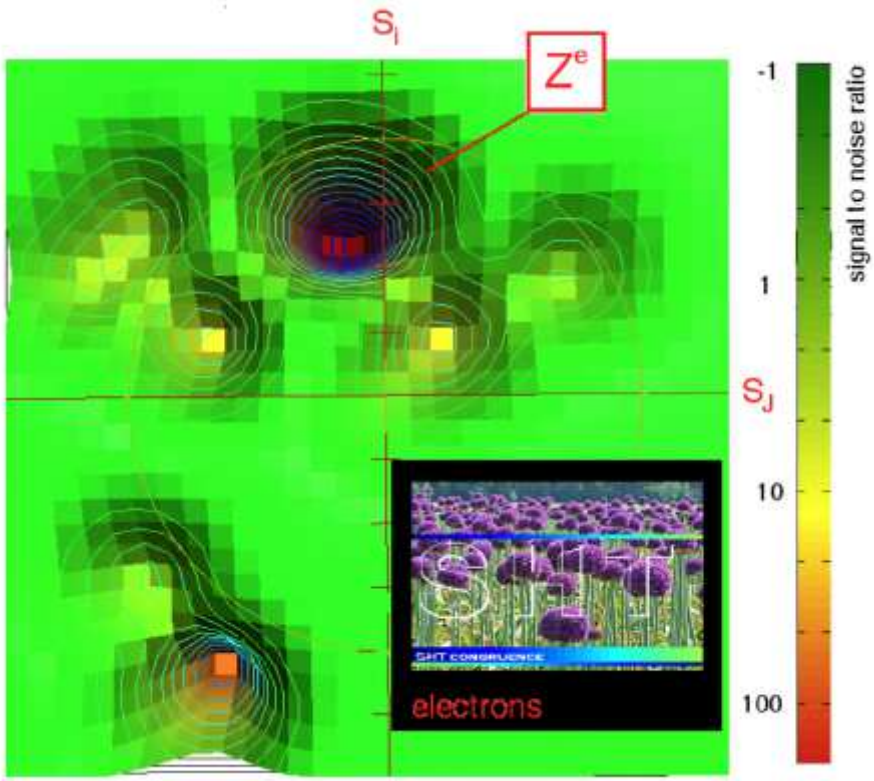

Figure 10

Level 1 - Data-Funnel section of the same ensemble of matrices (see fig. 9) relating to DA□NE electron synhcrotron radiation emission data. The absolute minimum Ze identifies the best values of the ensemble.

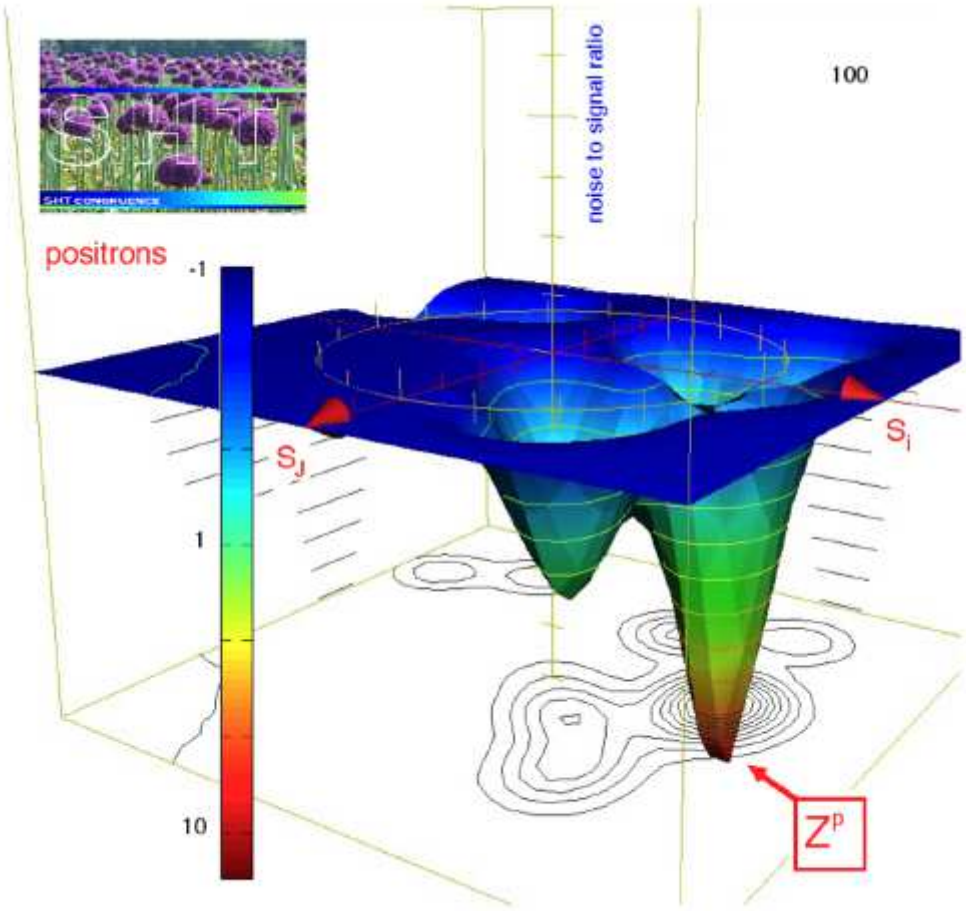

Figure 11

Level 1 - Data-Funnel of an ensemble of matrices relating to DA□NE positron synhcrotron radiation emission data. The absolute minimum Zp identifies the best values of the ensemble.

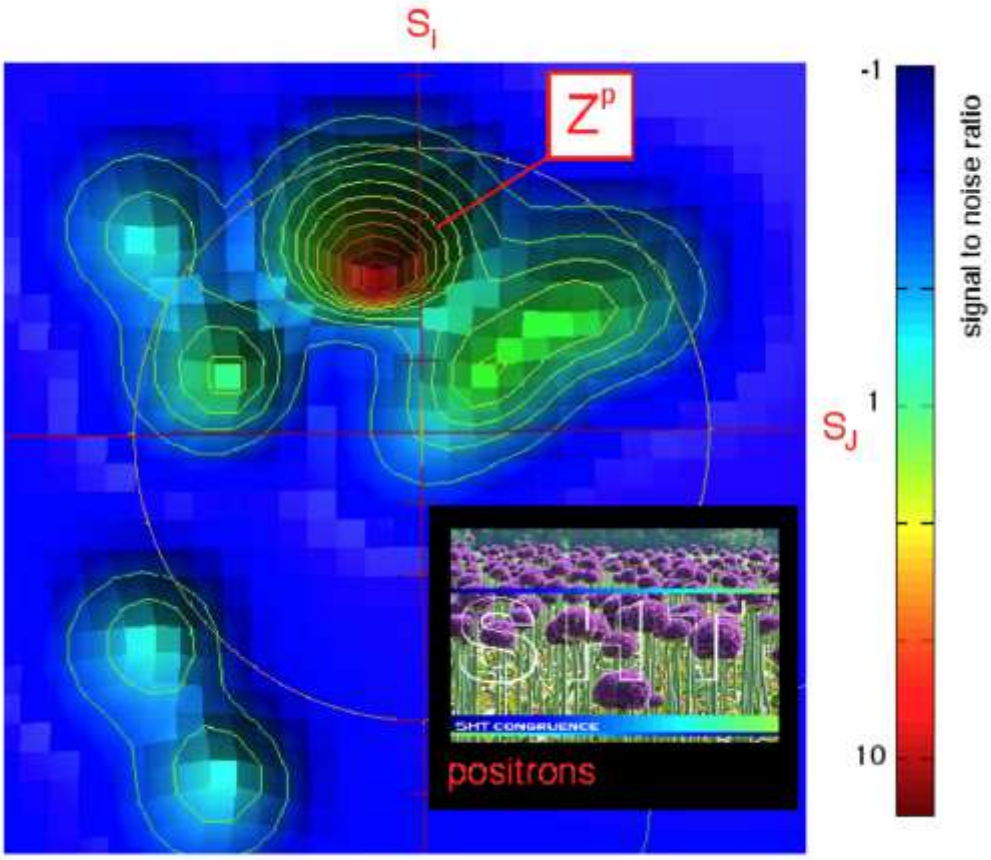

Figure 12

Level 1 -Data-Funnel section of the same ensemble of matrices (see fig. 11) relating to DA□NE positron synhcrotron radiation emission data. The abs

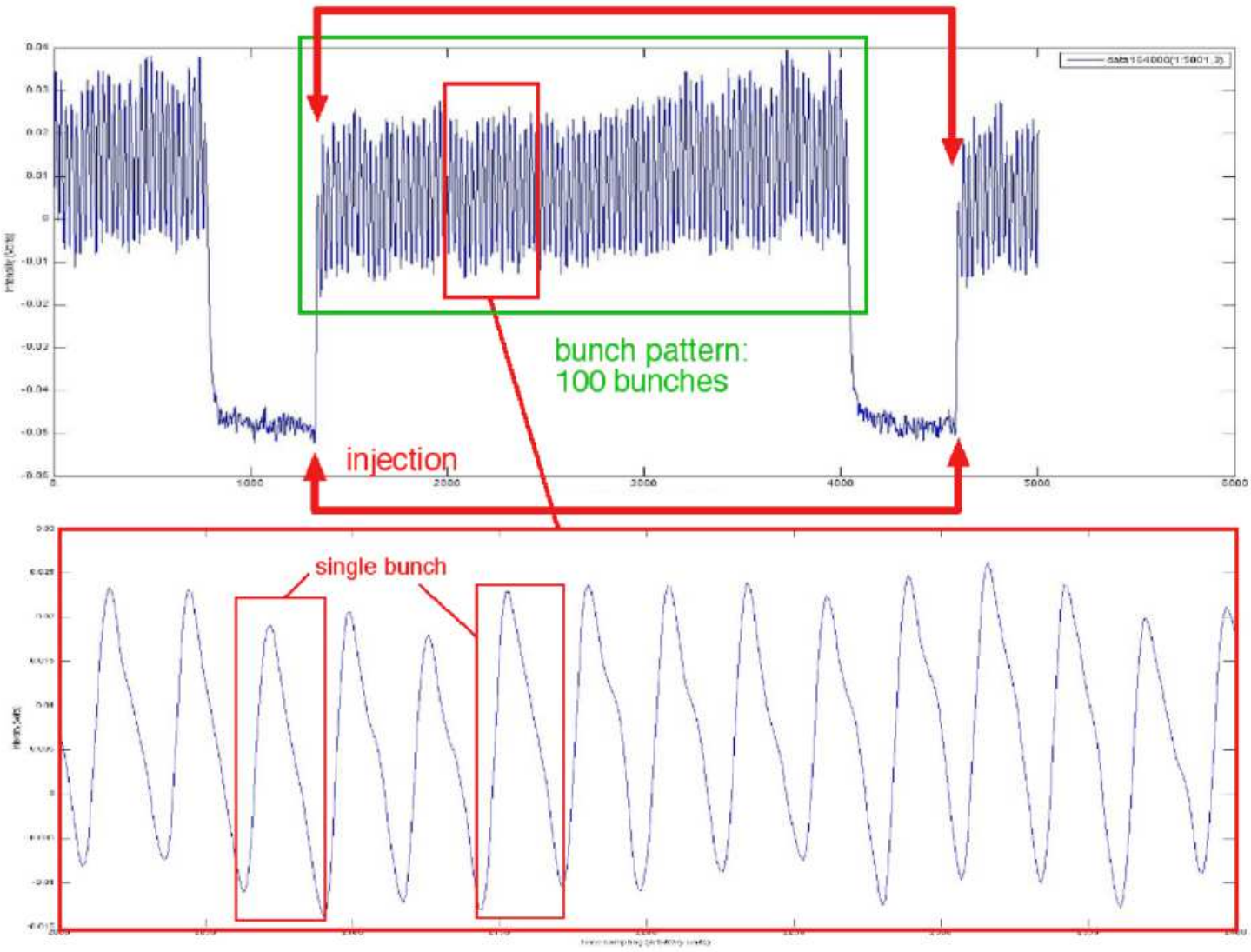

Figure 13

Typical signal of the IR synchrotron radiation emission photo-detector response, corresponding to a complete filling of 100 bunches of DA□NE electrons (highlighted by red arrows).

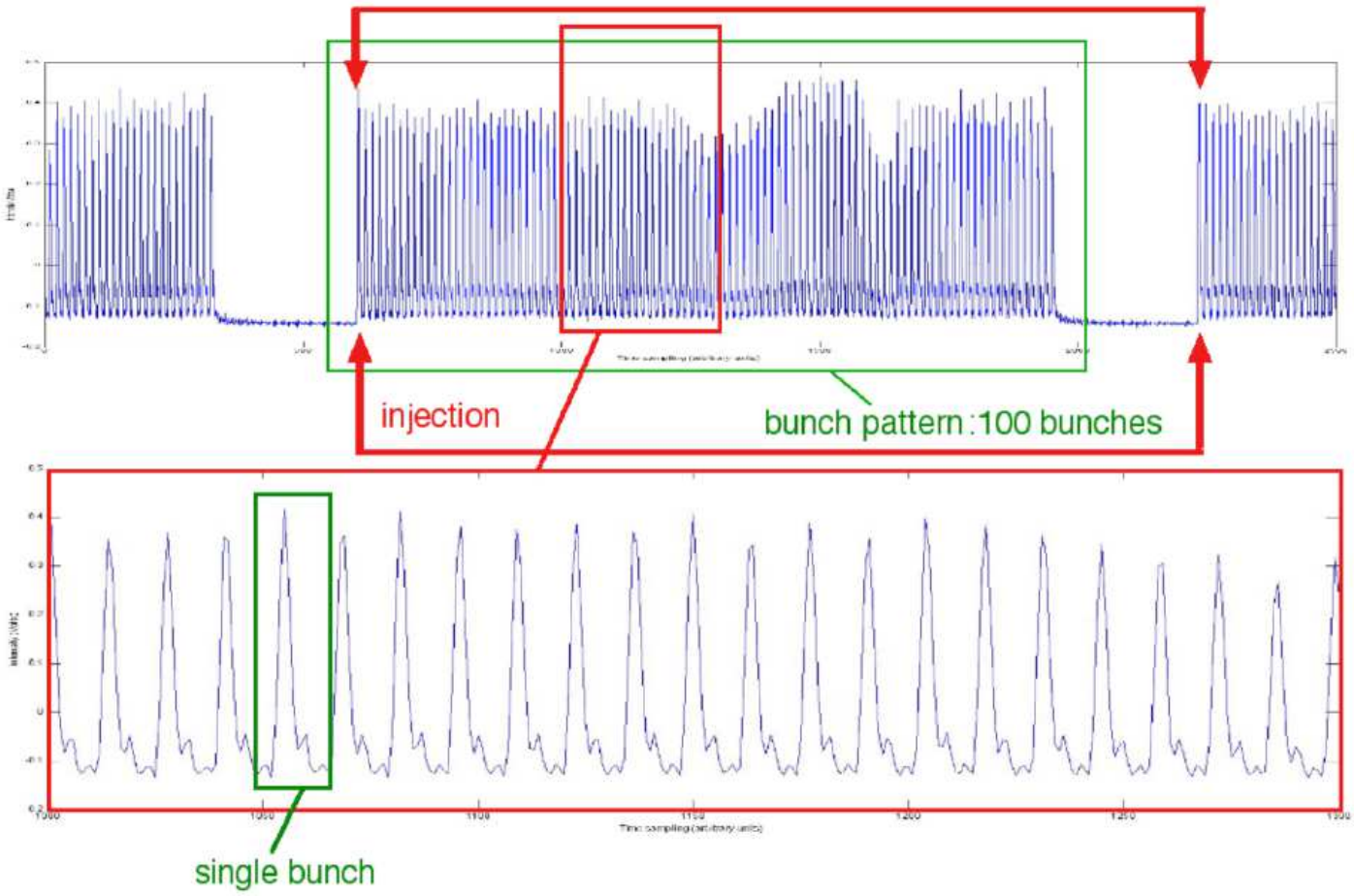

Figure 14

Typical signal of the IR synchrotron radiation emission photo-detector response, corresponding to a complete filling of 100 bunches of DA□NE positrons (highlighted by red arrows).

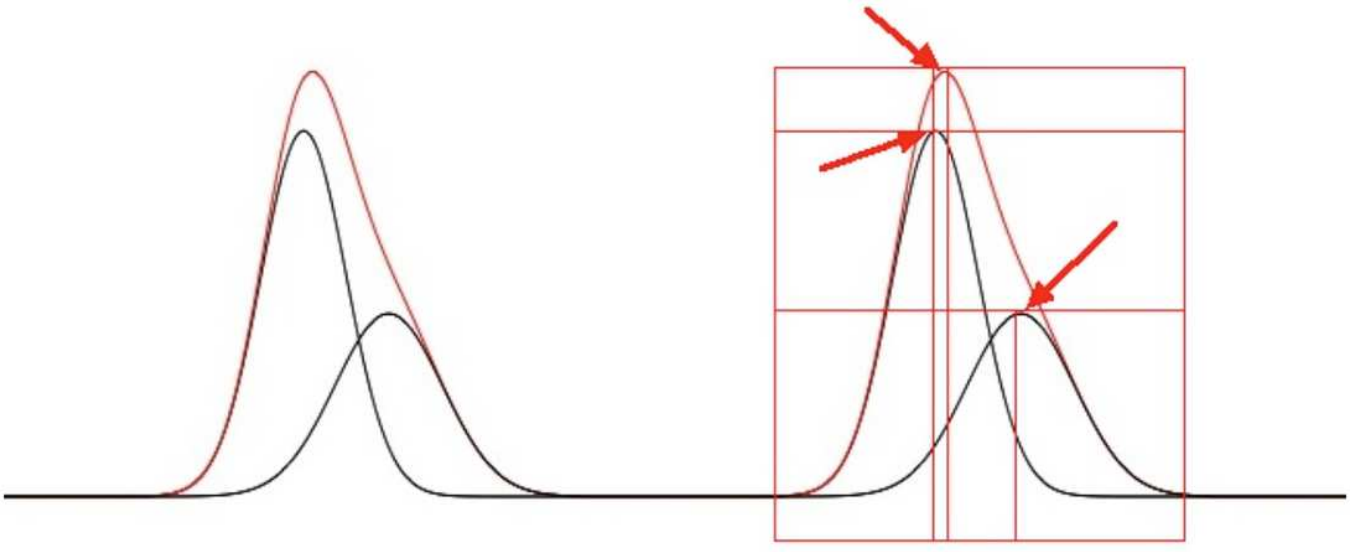

Figure 15

Typical systematic error of the automatic tool "peak-finder", offered by commercial spectral analysis software. The software is blind to the components (hidden) in the convolution (black), so it overestimates the intensity and misses the width and the center.

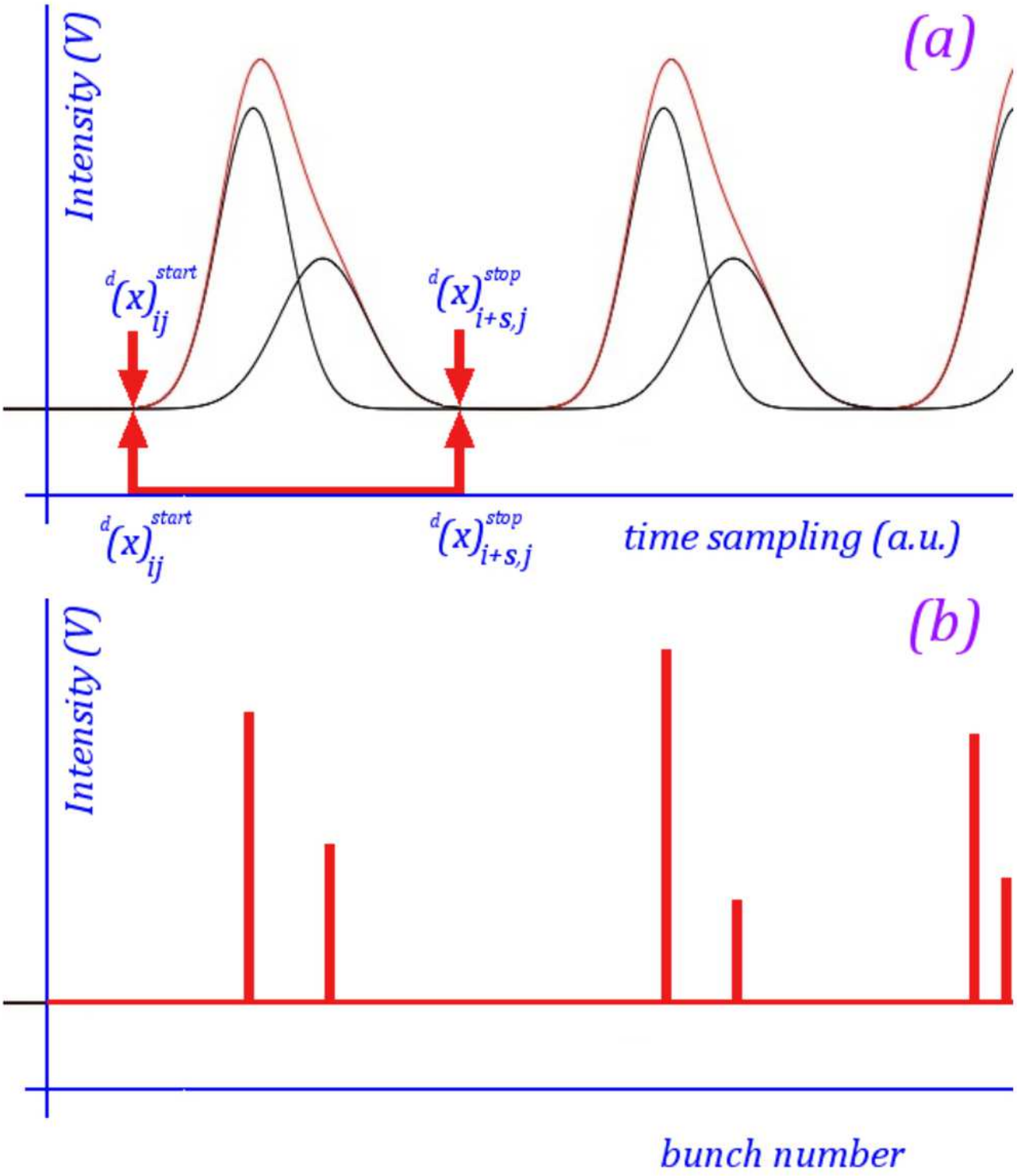

Figure 16

Transformation of time intervals and delays. Figure (a) Sampling and definition of the time intervals between the radiation emission of each bunch (DA□NE electrons). Figure (b) histographic sequence of

intensity sampling.

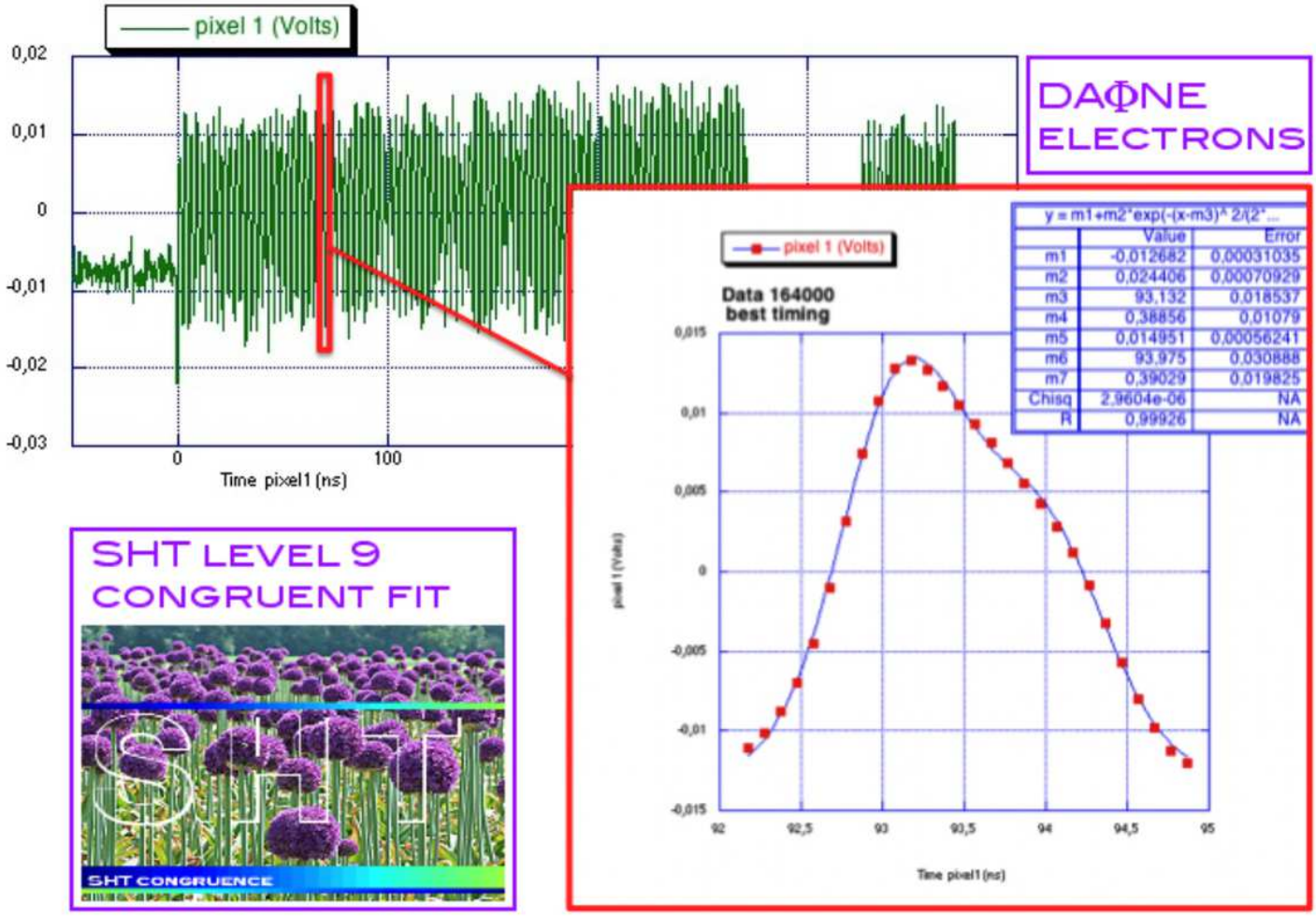

Figure 17

SHT level 9 regression with a double Gaussian on a typical IR synchrotron radiation (pixel 1) double emission profile ("main" and "delayed") of a bunch of DA□NE electrons.

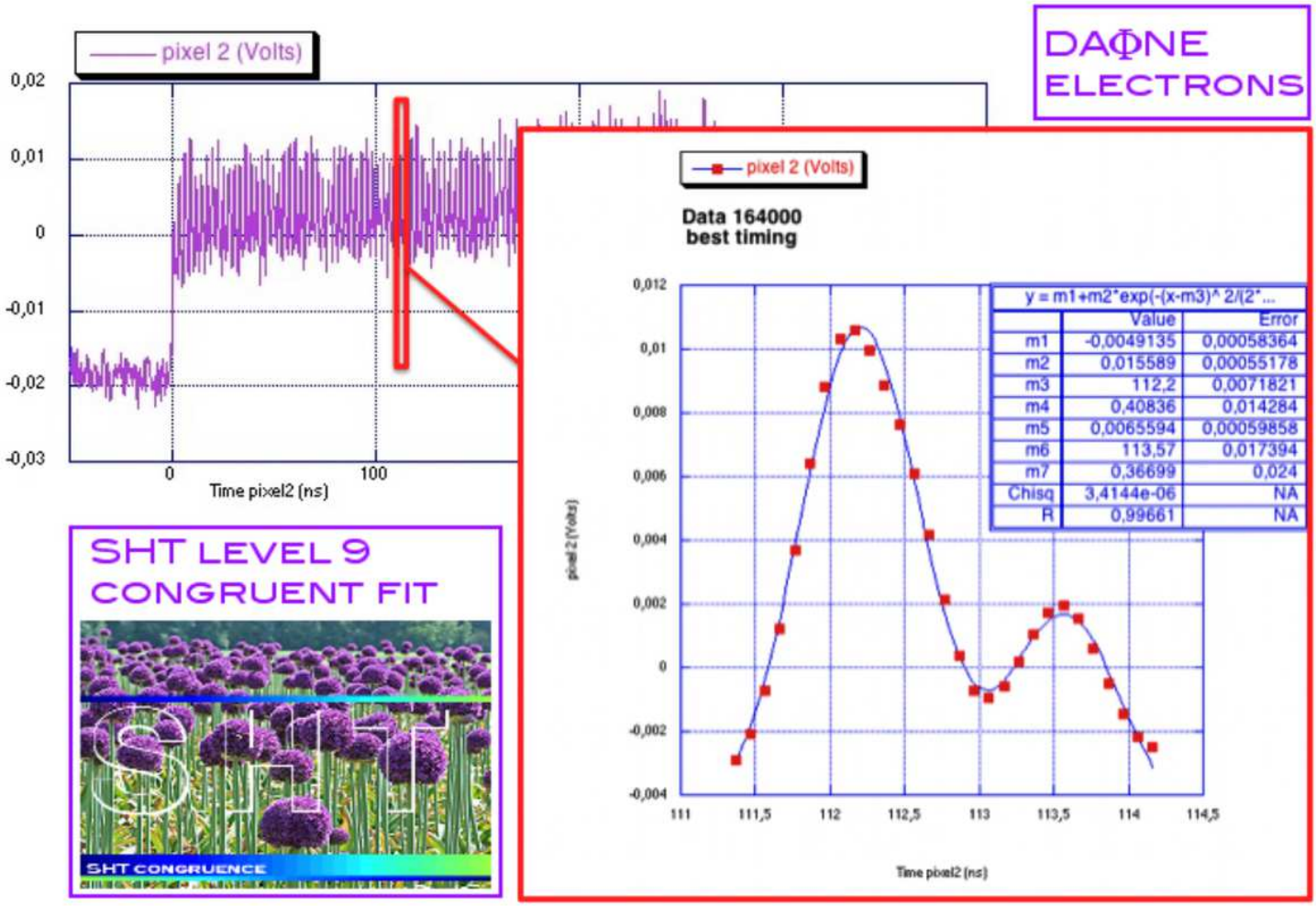

Figure 18

SHT level 9 regression with a double Gaussian on a typical IR synchrotron radiation (pixel 2) double emission profile ("main" and "delayed") of a bunch of DA□NE electrons.

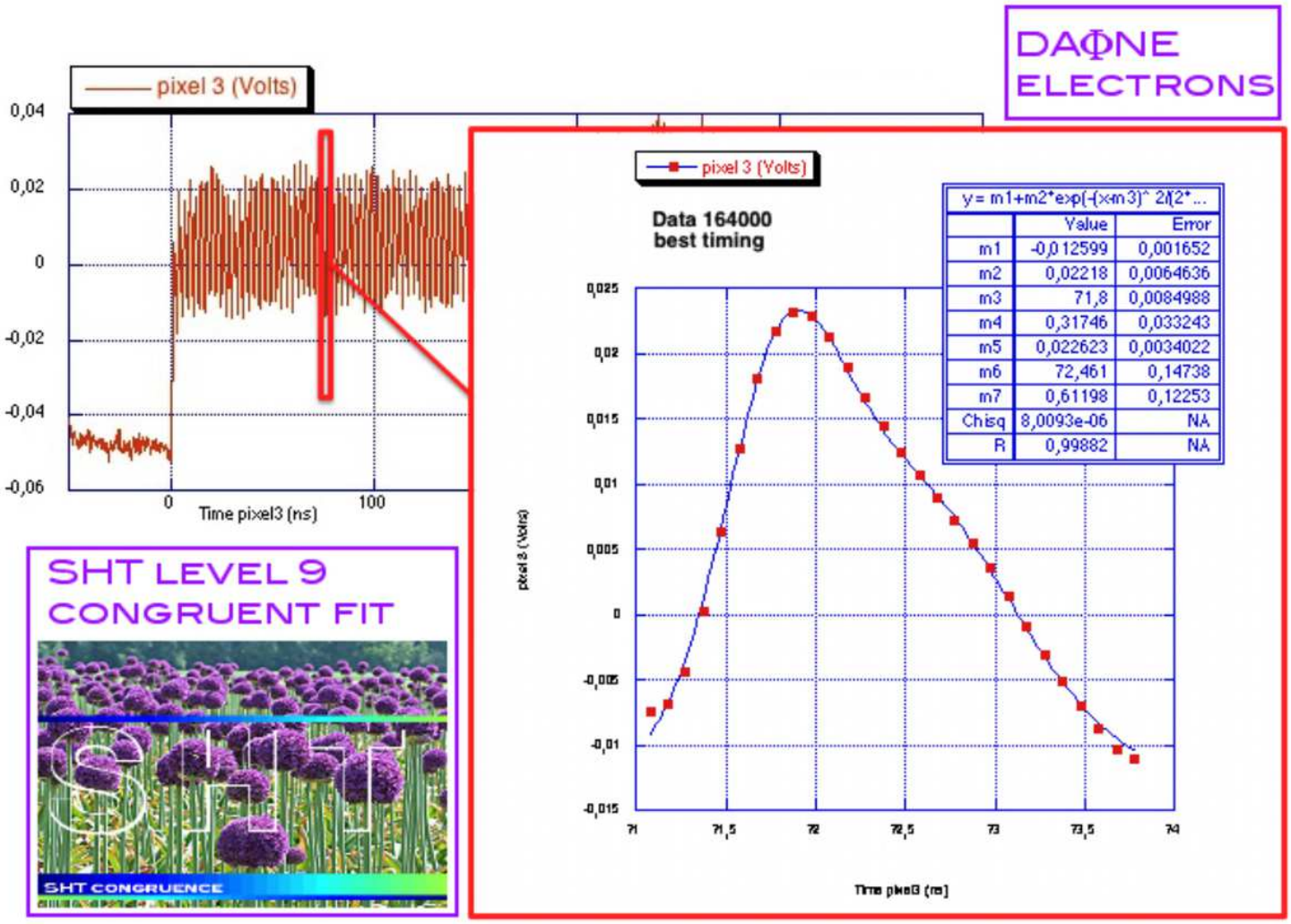

Figure 19

SHT level 9 regression with a double Gaussian on a typical IR synchrotron radiation (pixel 3) double emission profile ("main" and "delayed") of a bunch of DA□NE electrons.

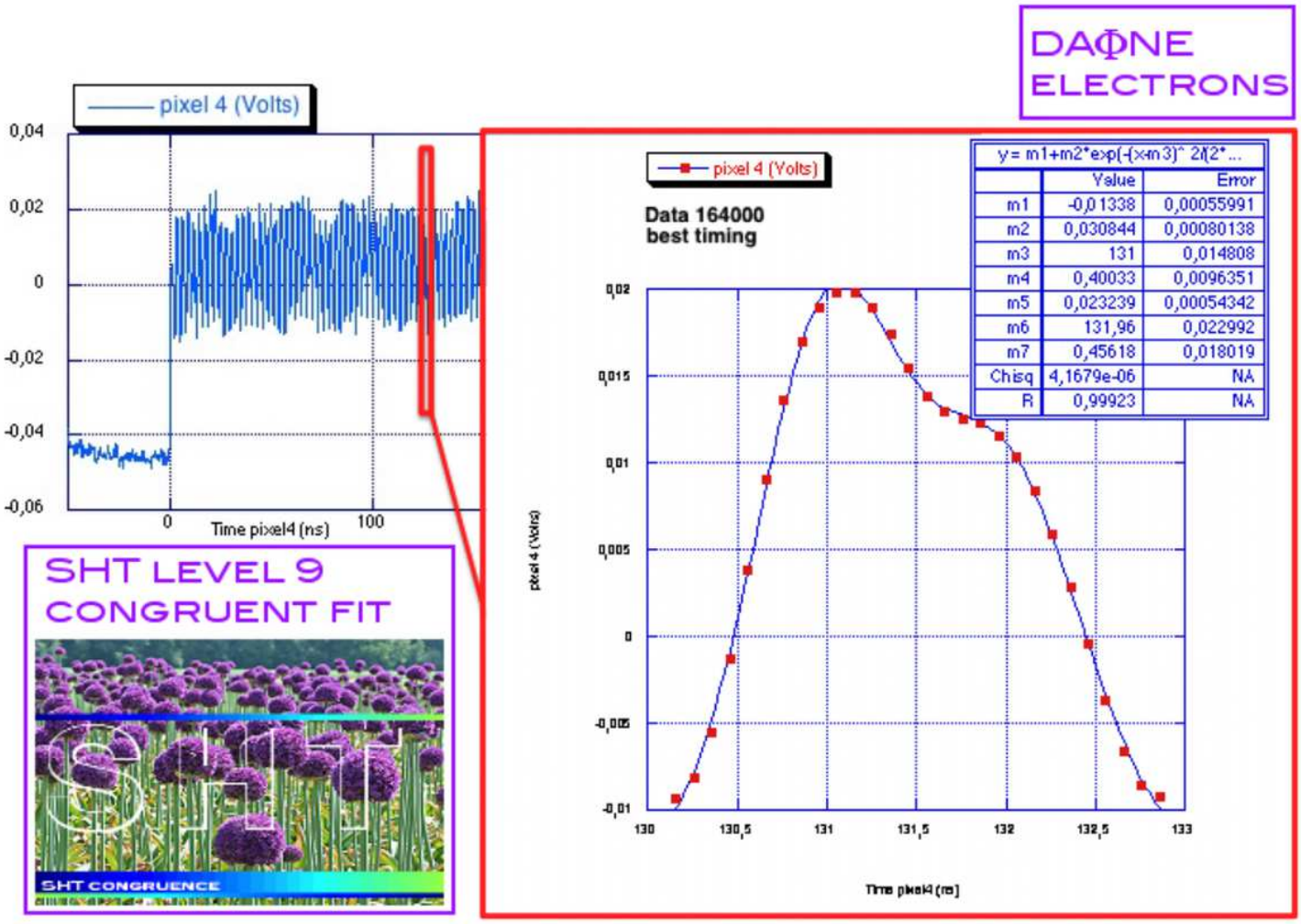

Figure 20

SHT level 9 regression with a double Gaussian on a typical IR synchrotron radiation (pixel 4) double emission profile ("main" and "delayed") of a bunch of DA□NE electrons.

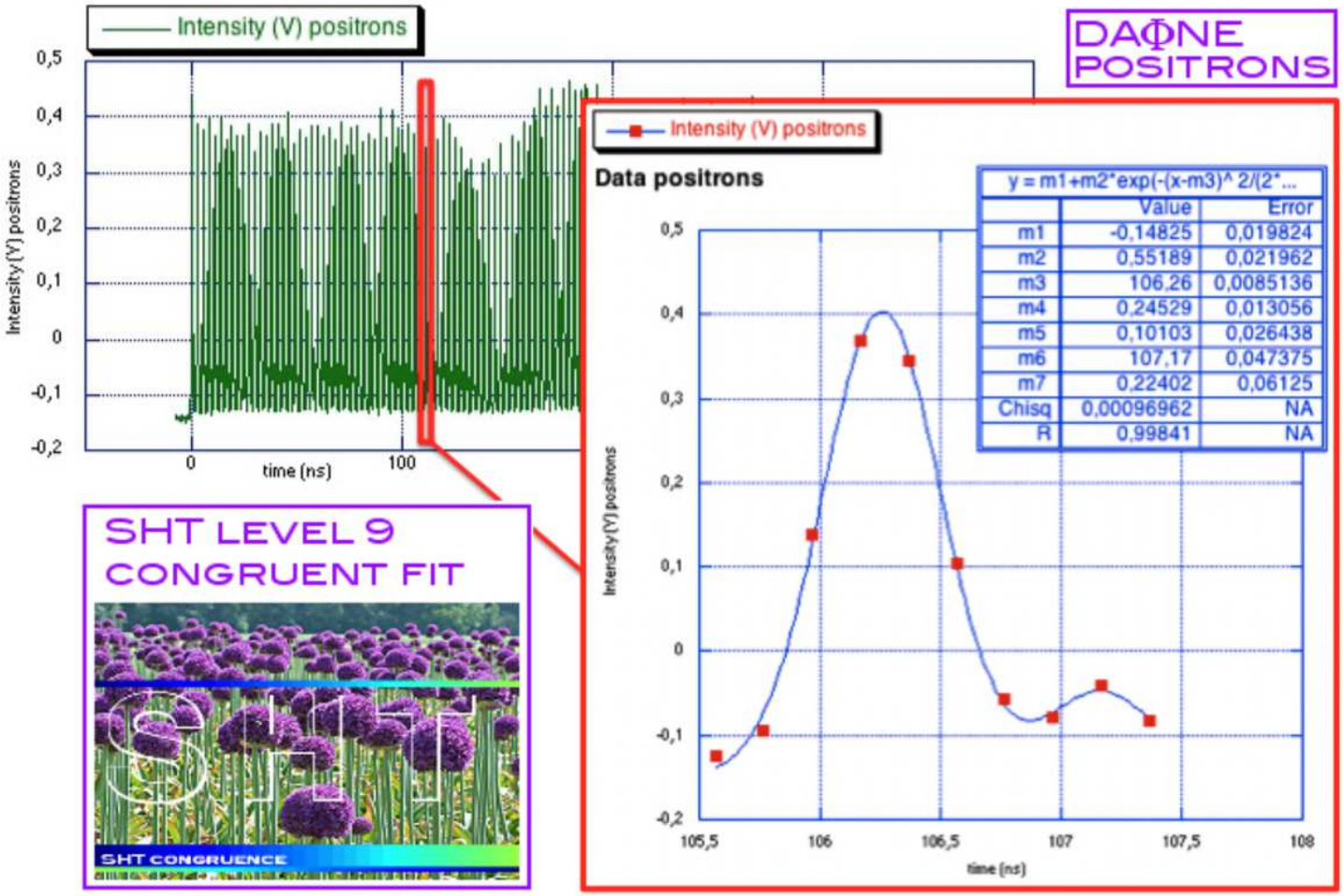

Figure 21

SHT level 9 regression with a double Gaussian on a typical IR synchrotron radiation double emission profile ("main" and "delayed") of a bunch of DA□NE positrons. Single photo-detector configuration.

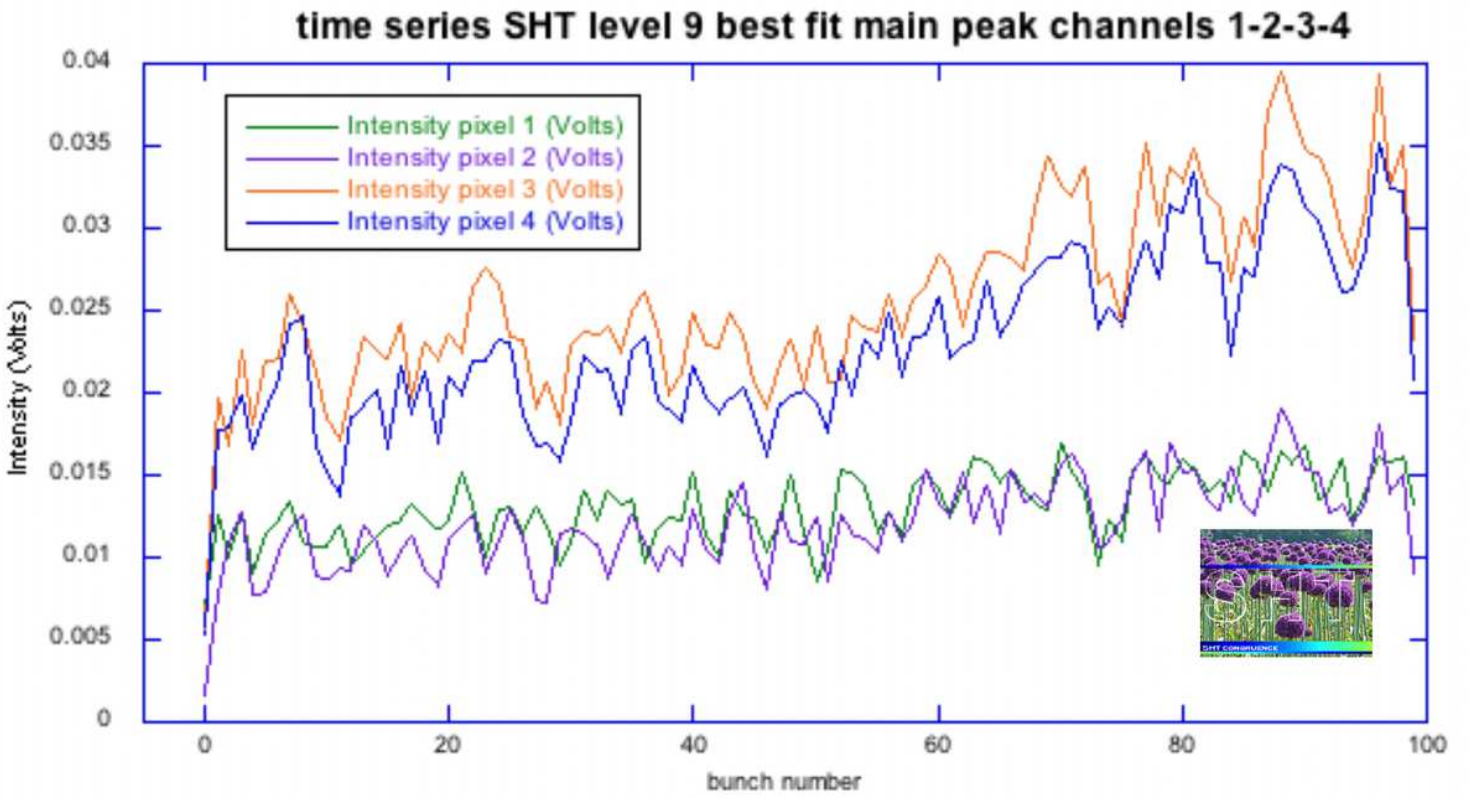

Figure 22

Comparative and summary diagram of the 4 time series of the intensities (V) of the "main peaks" of IR synchrotron radiation emission of each bunch acquired by the MCT (pixel) 1-2-3-4 photo-detectors and ordered in the sequence of 100 bunches of a complete DA□NE electron filling.

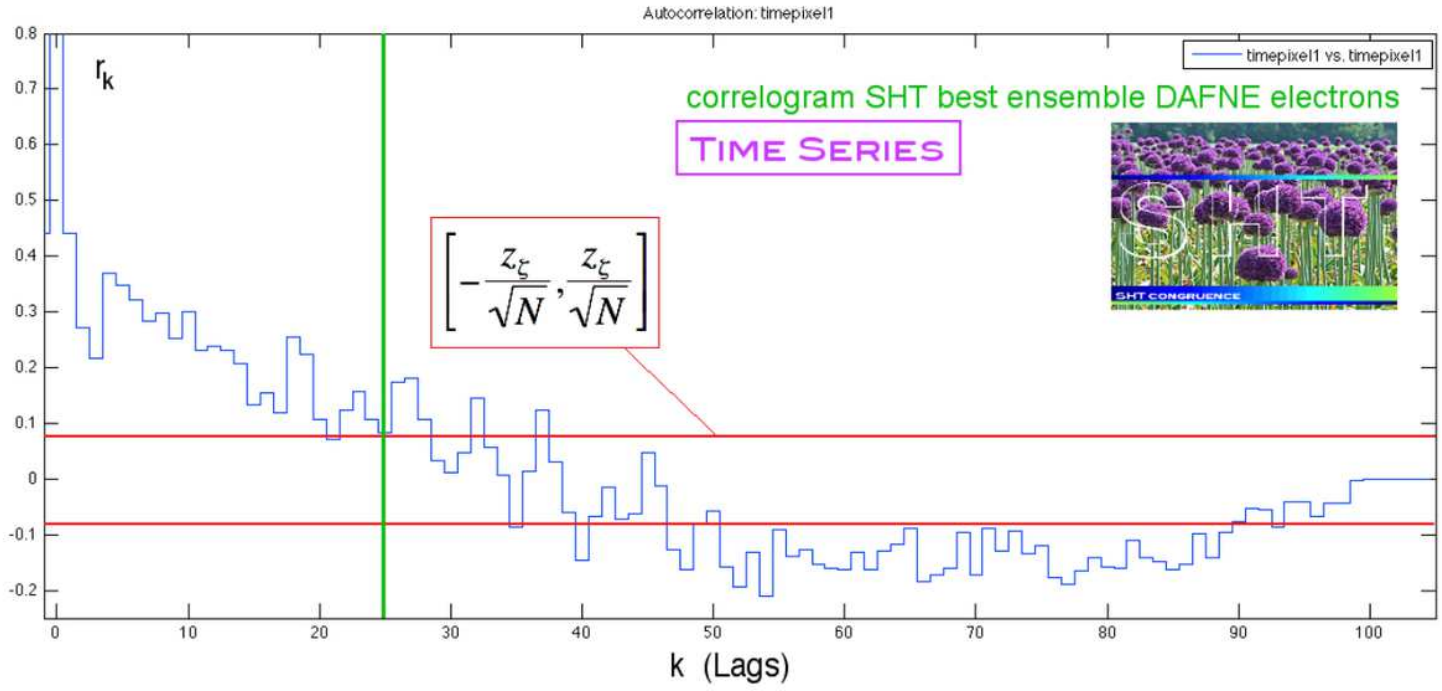

Figure 23

Correlogram (main peaks) of a best ensemble Ze. Confidence bands are highlighted in red. The marker ("boundary-lag") is marked in green at T / 4 (DA□NE electrons).

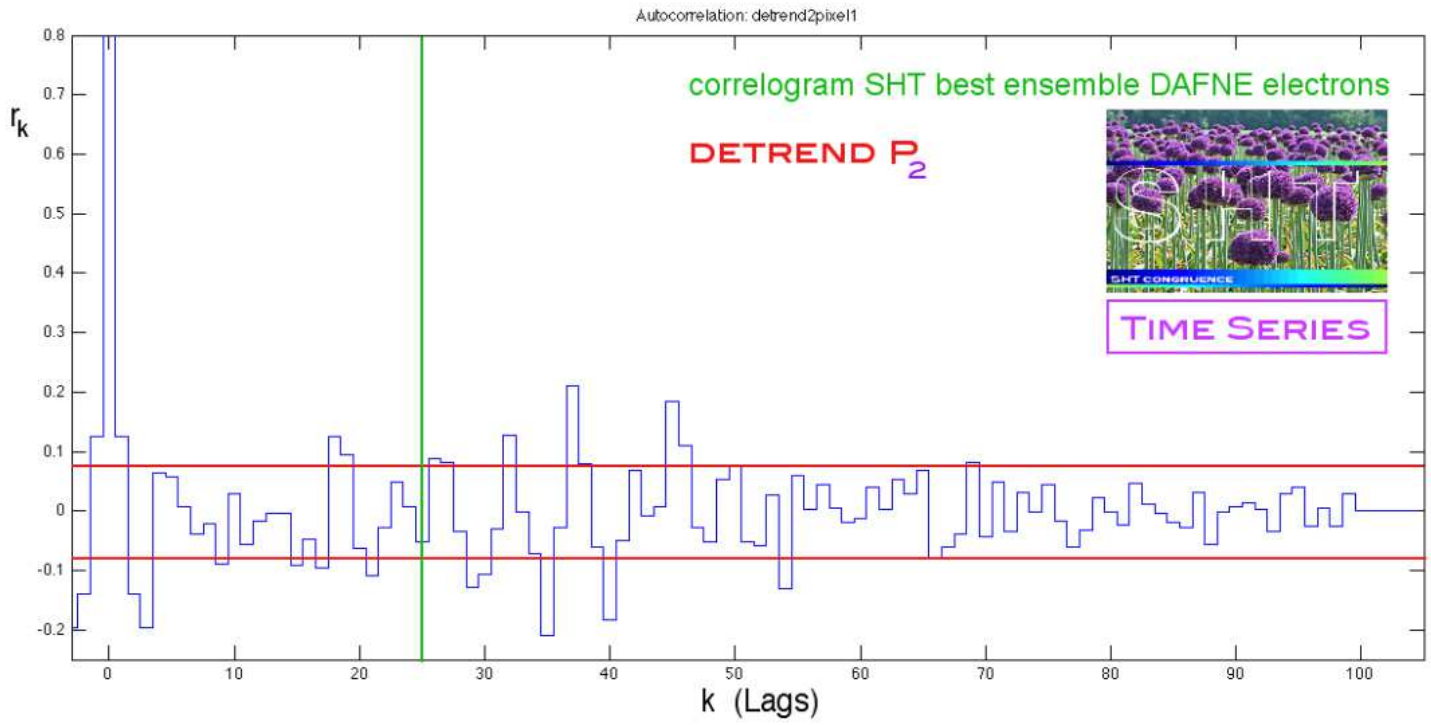

Figure 24

Correlogram of the residues of the Zt series (detrend P2 (t)) DA□NE electrons.

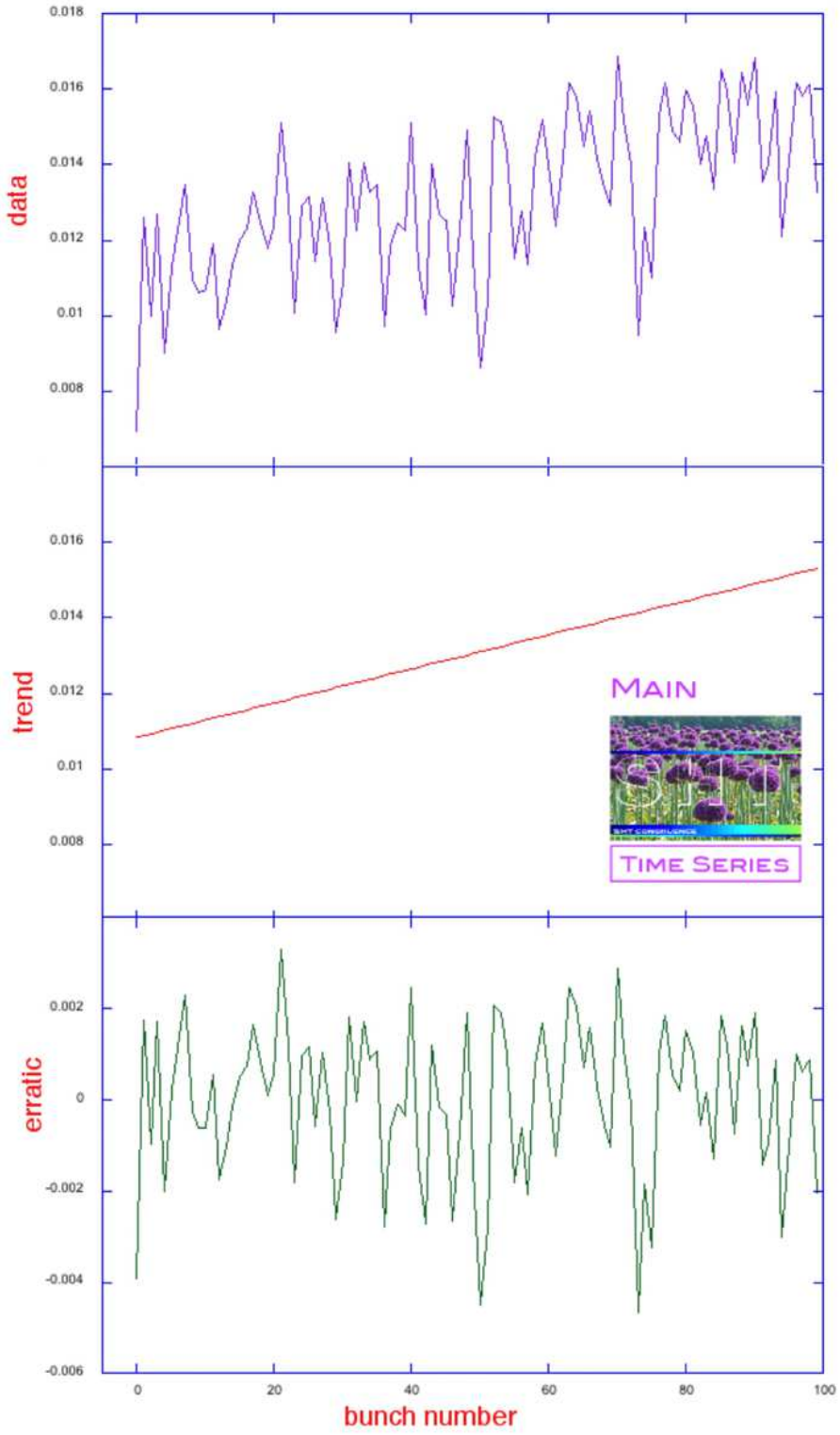

Figure 25

Comparative and summary diagram of the decomposition of the Zt series (main component - DA□NE electrons)

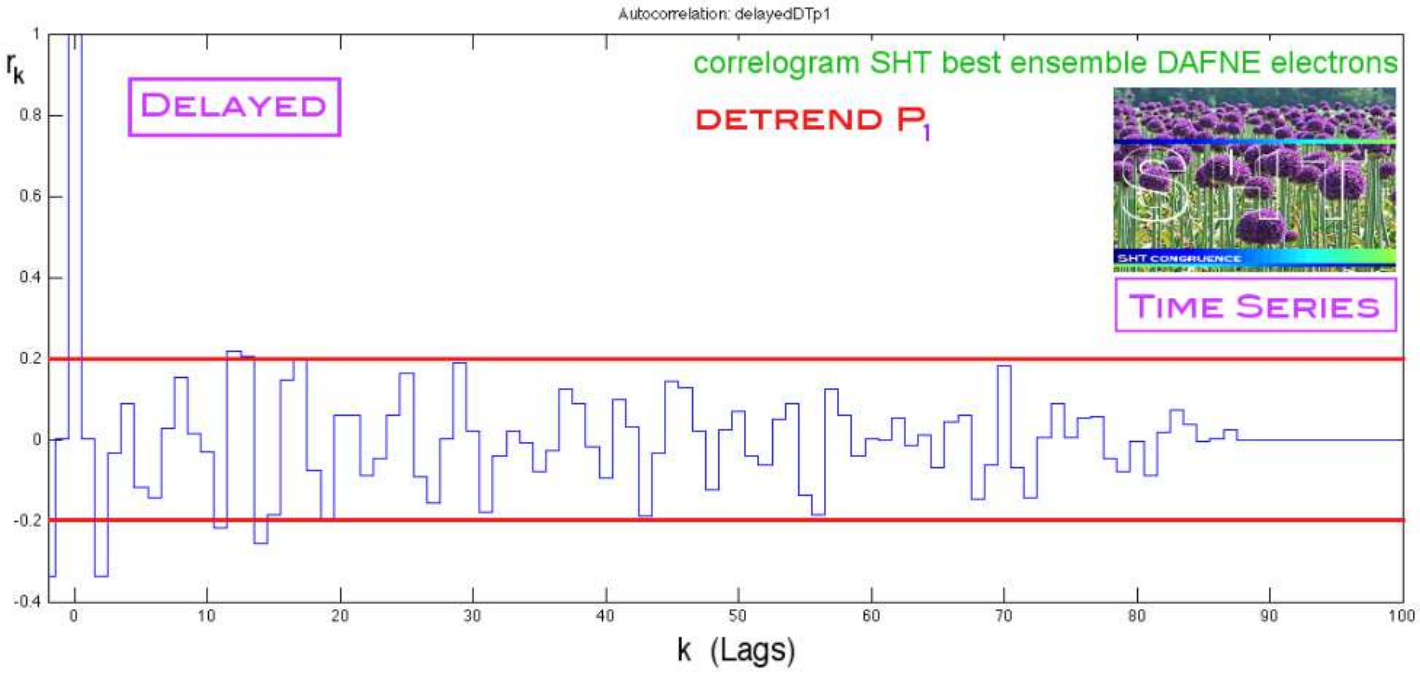

Figure 26

Correlogram of the residues of the Zt series (detrend P1 (t)). Delayed component - DA□NE electrons.

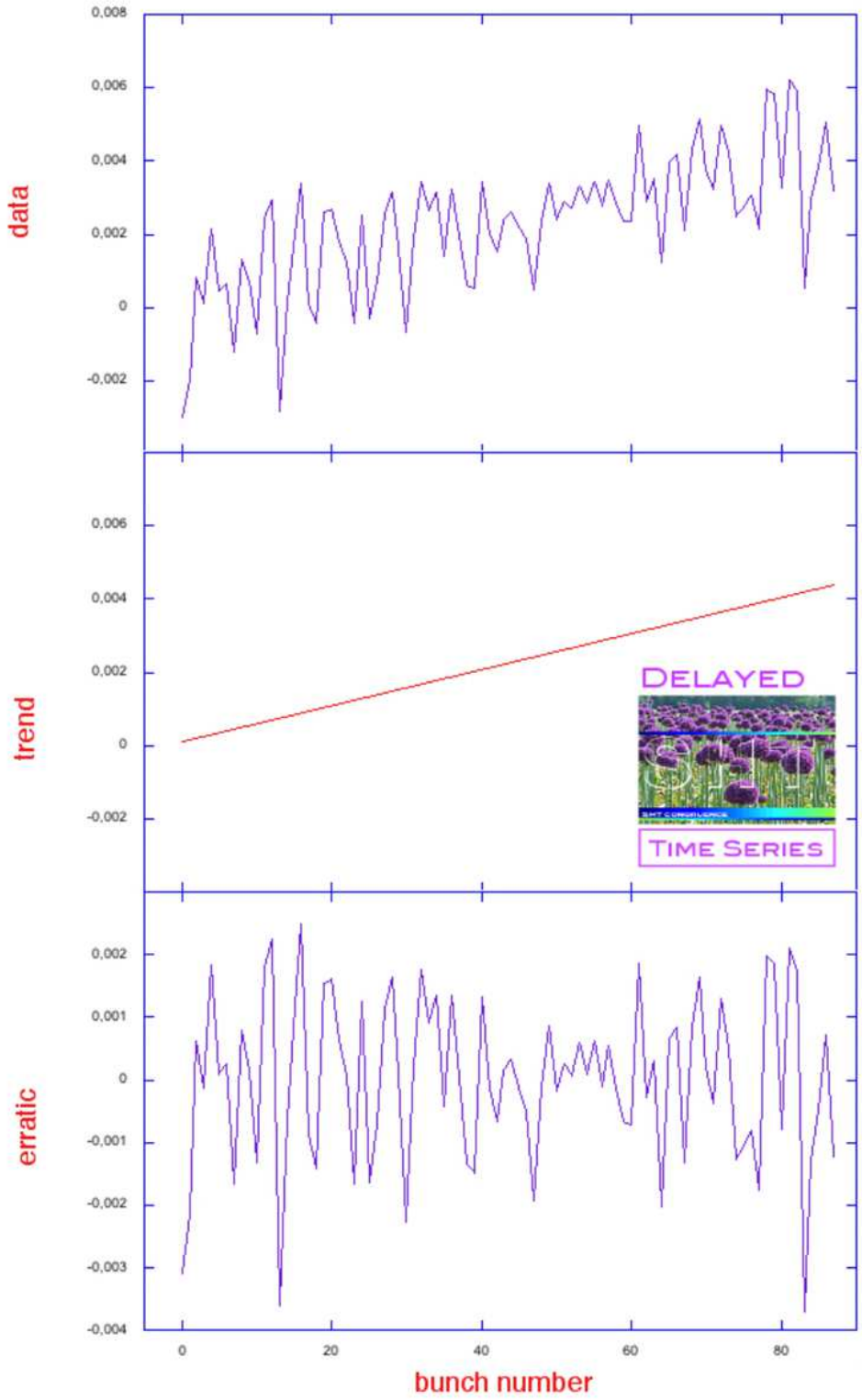

Figure 27

Comparative and summary diagram of the decomposition of the Zt series ("delayed" component - DA□NE electrons)

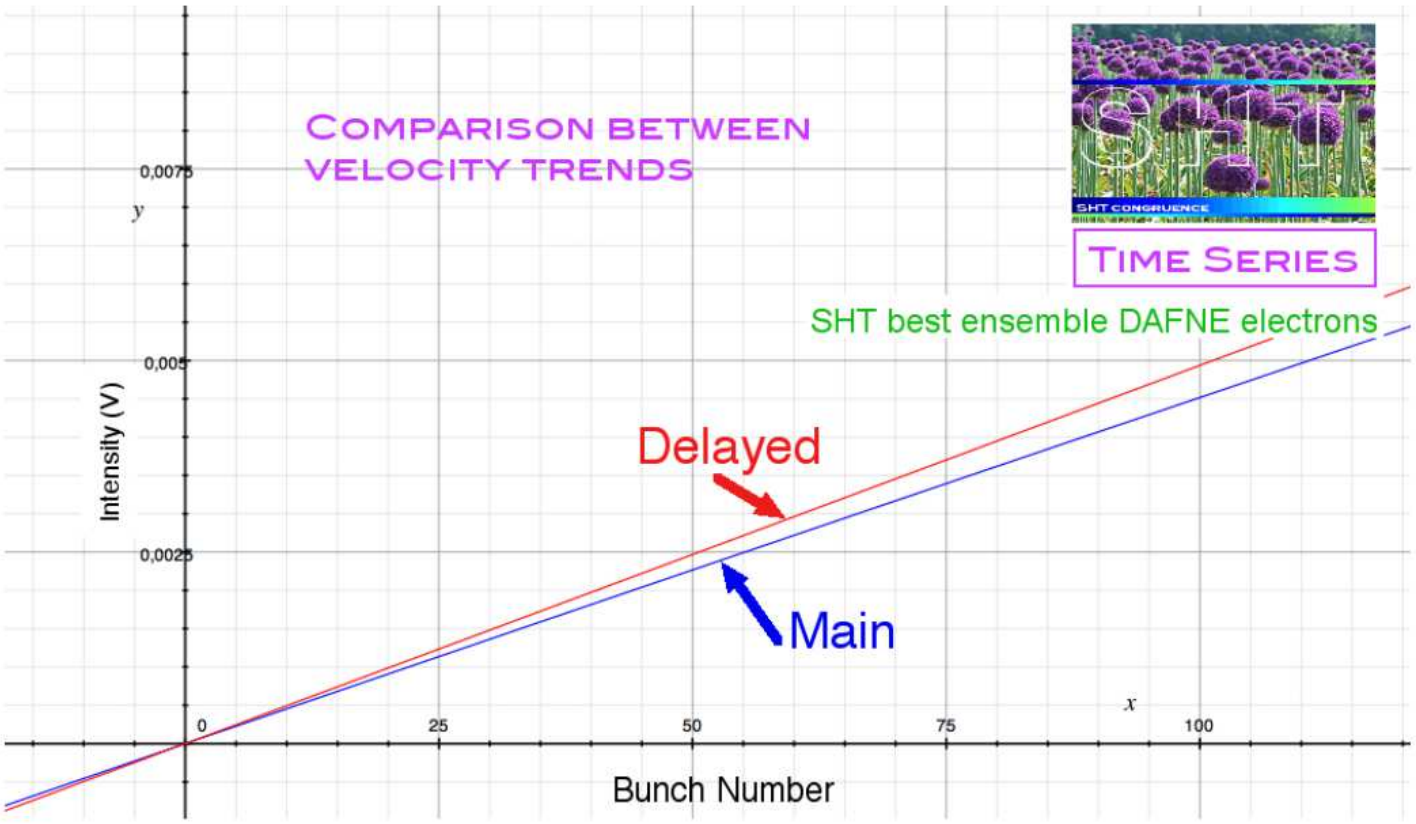

Figure 28

Comparison between the trend models: "main" component vs "delayed". DA□NE electrons.

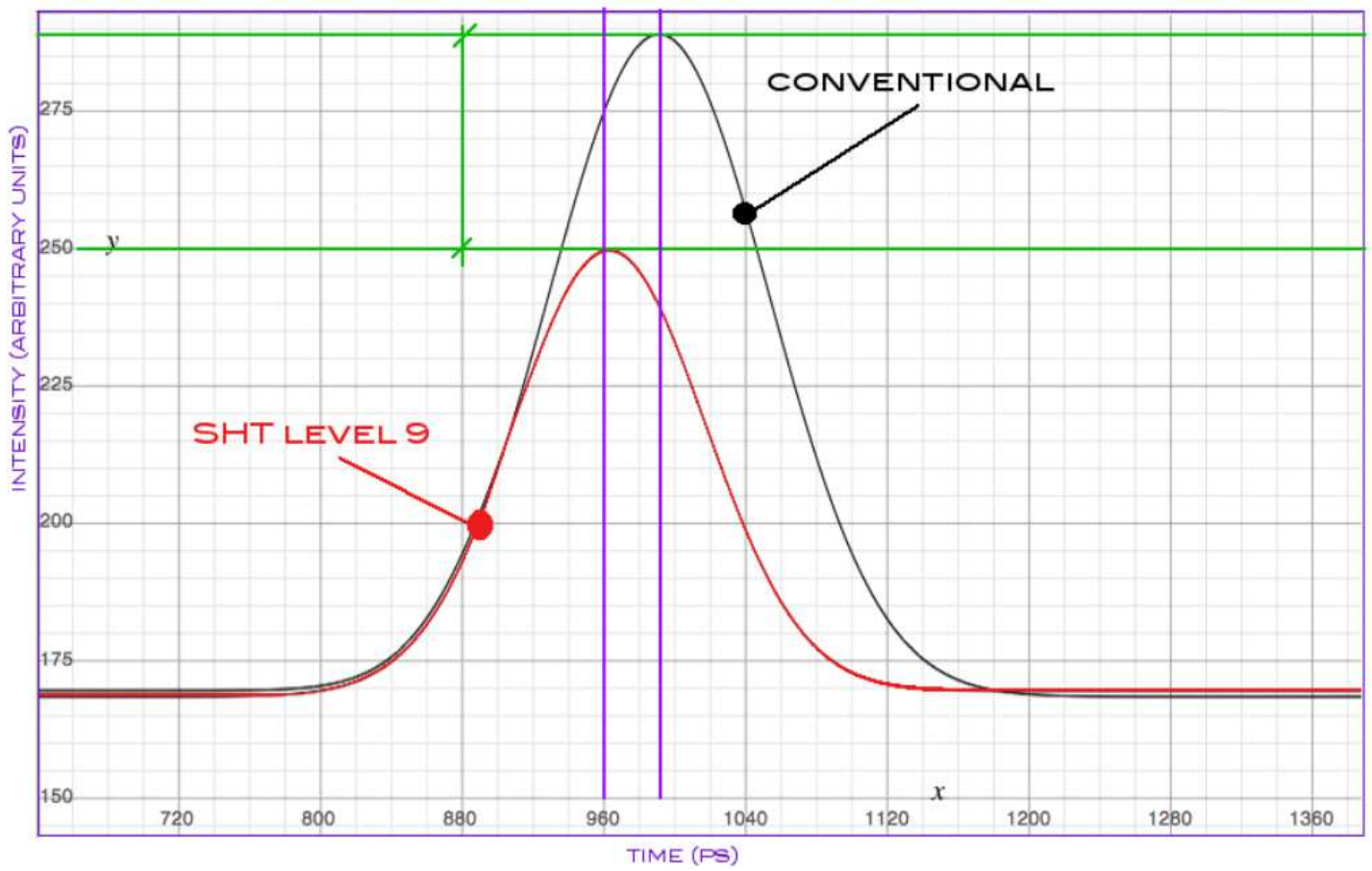

Figure 29

DA□NE positrons. Cartesian representation of the discrepancies between "conventional" interpolation (courtesy of M. Zobov, Frascati National Laboratories) and SHT level 9. As can be seen, "conventional" interpolation leads to an overestimation of both intensity, center and width. Neglecting the contribution of the delayed component therefore leads to a significant systematic error.

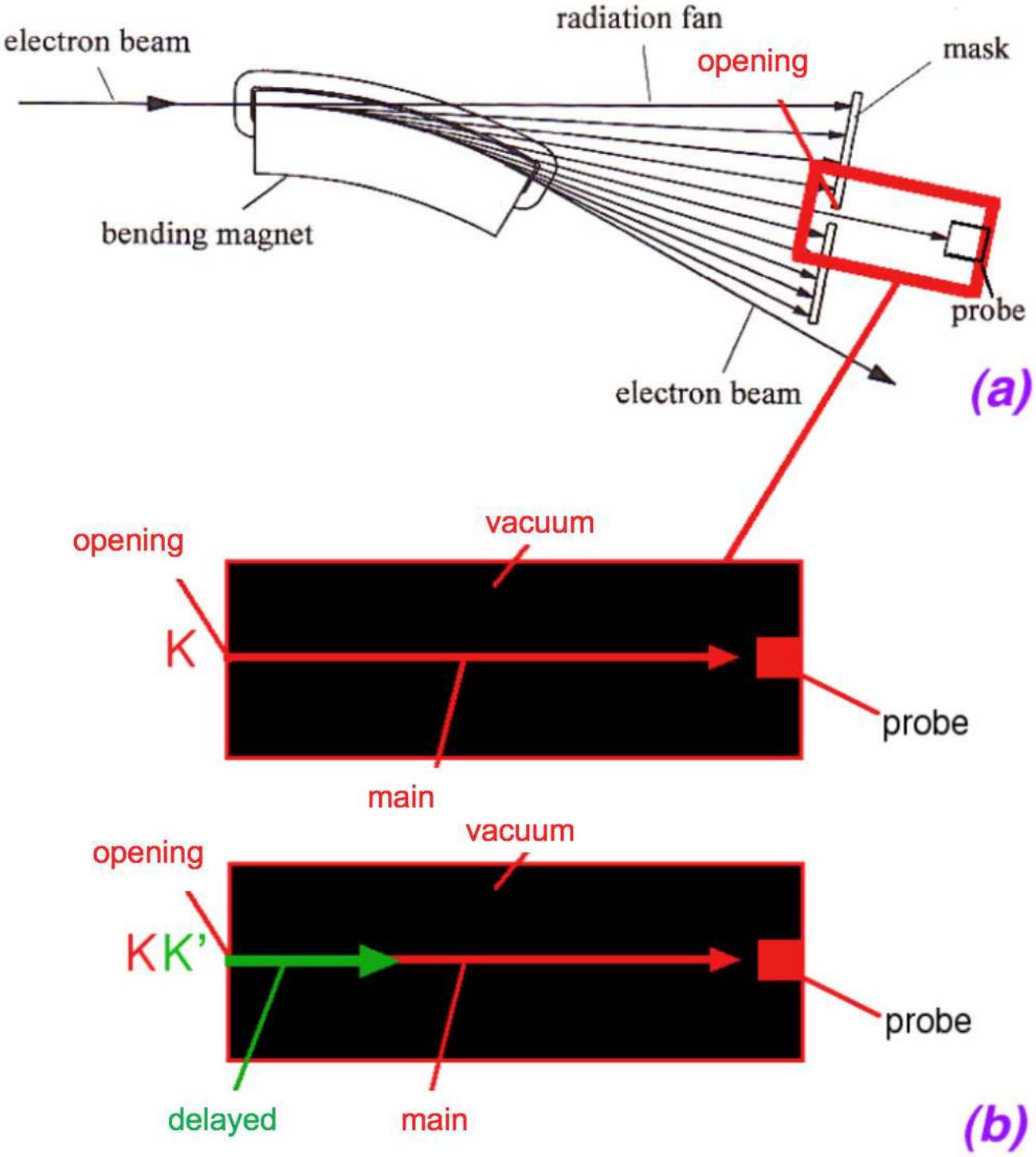

Figure 30

(a) SR emission by an electron (positron) beam during accelerated motion in a bending magnet. (b) Scheme of the emission of two light signals ("main" and "delayed") from the same source (opening) K. (Schematics modified after A. Hofmann [13])

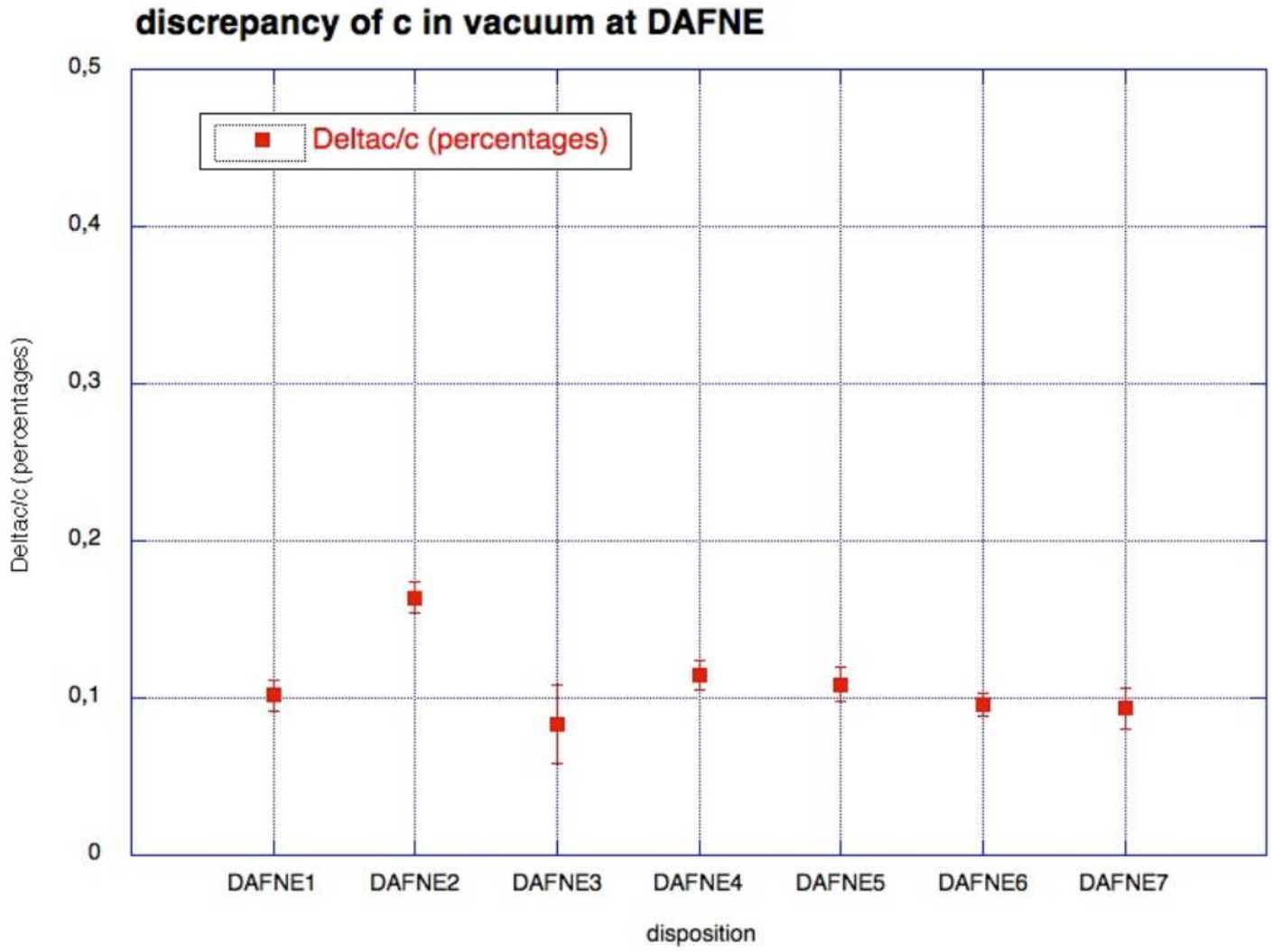

Figure 31

Discrepancies δc/c in the case of DAΦNE (electrons)

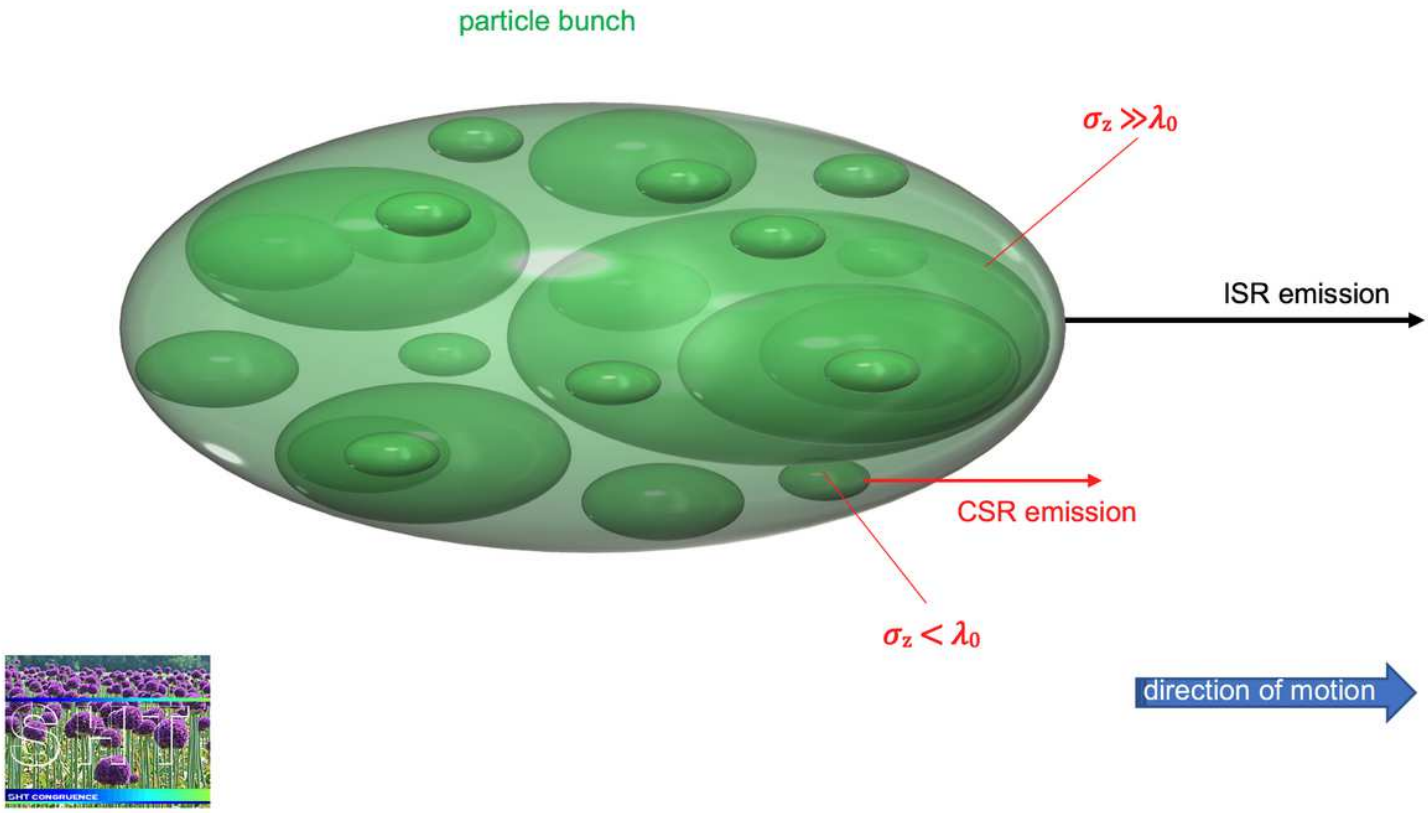

Figure 32

Fractal Nematic Mesophase. Snapshot of a SHT simulation

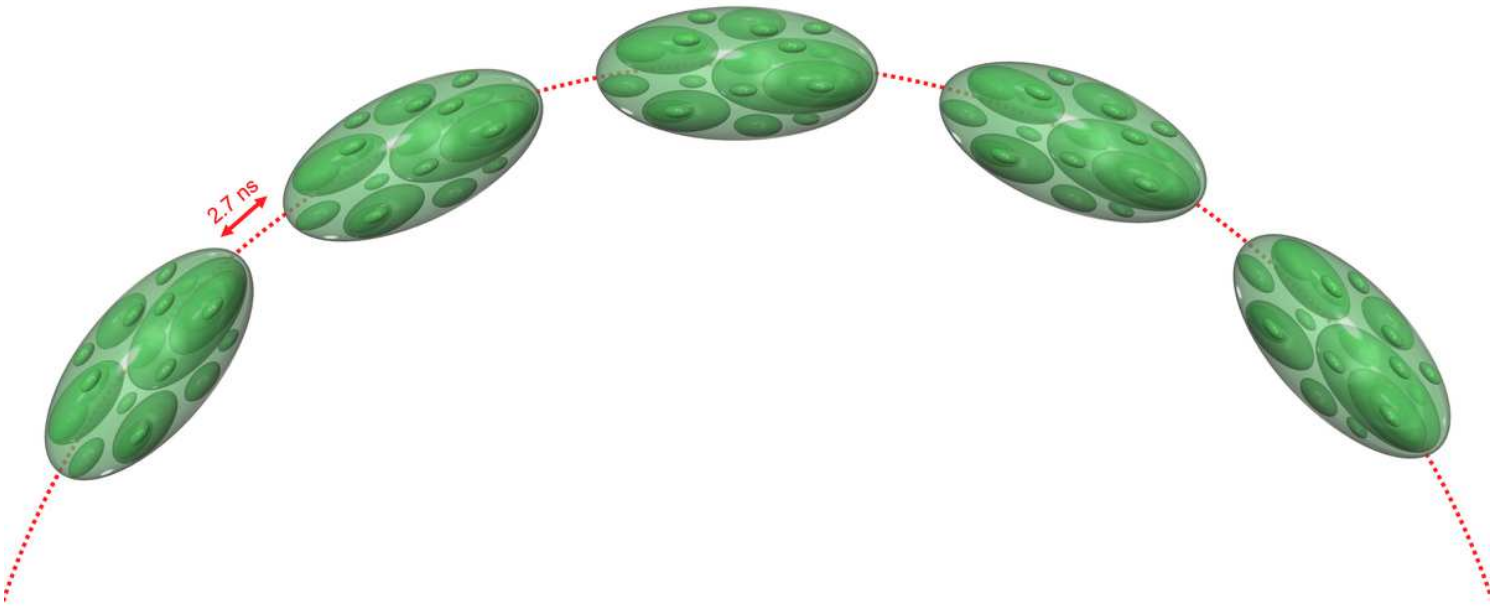

Figure 33

Motion of a "fractal nematic mesophase" of particles in a DA□NE bending magnet.